

Tuning from unipolar (p-type or n-type) to ambipolar charge transport efficiency in bowl-shaped perylene-derivatives: a DFT study

Suryakanti Debata,[†] Nataliya N Karaush,[‡] and Sridhar

Sahu^{*,†}

[†]*High Performance Computing lab, Department of Physics, Indian Institute of Technology
(Indian School of Mines) Dhanbad, India*

[‡]*Department of Chemistry and Nanomaterials Science, Bohdan Khmelnytsky National
University, Cherkasy, Ukraine*

E-mail: sridharsahu@iitism.ac.in

Abstract

A series of bowl-shaped dicyclopenta perylene (DCPP) derivatives have been theoretically constructed by indeno-substitution at the peri-positions of DCPP, and suitably functionalizing with aza-, fluoride and imide-groups to enhance the electron transport behavior in the materials. To further ensure the solubility and stability of these organic compounds, we incorporated triethylsilylethynyl (TES) groups in the designed structures. The factors such as degree of aromaticity, electronic structure, molecular packing motif, intermolecular charge coupling, and charge transfer rate are essential in determining the charge transporting ability. The low-lying LUMO-levels (< -4.0 eV) and high electron affinities (> 3.0 eV) of a few DCPPs ensure efficient electron injection from the metal electrodes. These molecules are arranged in bowl-in-bowl columnar packing, which is suitable for facilitating the intermolecular charge transport in the crystal. As a result, we observed enhanced hole-transport behavior in DCPP-9 ($\mu_h = 6.296$ cm²V⁻¹s⁻¹), electron transport in DCPP-TES-6 ($\mu_e = 0.142$ cm²V⁻¹s⁻¹) and ambipolar nature of DCPP-12 and DCPP-TES-12. The DCPP-derivatives are also optically active in the UV-visible region, which is confirmed from the TD-DFT analysis. Inspired from their non-centrosymmetric molecular geometry and optical activity, we also investigated their non-linear optical (NLO) responses, which may pave their way towards applications in photonics and optoelectronics.

1. Introduction

Bowl-shaped polycyclic aromatic hydrocarbons (PAHs) (commonly known as buckybowl or π -bowls) are the open shell structures containing both the convex and concave surfaces in its curved geometry. In the last two decades, use of corannulene and sumanene have been extensively studied in organic electronics (OE) research. These two important structures being the wreckages of C_{60} fullerenes, behave in the similar way as the parent fullerenes in terms of their physicochemical properties.¹⁻⁴ For instance, corannulene exhibits a dipole moment of 2.1 debye, that helps in boosting the interfacial charge accumulation and hence the mobility of the system.⁵⁻⁷ Furthermore, the electronic and charge transport properties of the bowl-shaped organic semiconductors (OSCs) can be modulated by altering their molecular packing motifs.¹ Therefore, the bowl conformation is advantageous as compared to the planar PAHs for its ability of controllable molecular packing in building solids, bowl-to-bowl inversion (BWBI) feature, supramolecular assemblies, chiroptical activity, small HOMO-LUMO gap, and electronic conductivity. These interesting properties are originated from the distorted π -conjugation in the non-planar buckybowl, which gives rise to a minor overlapping of p-orbitals and emergence of s-orbital characteristic in the material.^{8,9}

Previously, the stereochemical properties of OSCs in OE were overlooked. However, the past few years witness the increasing interest towards contorted PAH-based OE.¹⁰⁻¹³ In this pursuit, a comparative study has been carried out by Fu *et al.*¹⁴, where the bowl-shaped (CorDI) compound was found to possess high electronic conductivity (mobility $\sim 0.05 \text{ cm}^2\text{V}^{-1}\text{s}^{-1}$). This is accredited to the low lying LUMO level of CorDI (-3.50 eV ; experimentally), which is comparatively lower than that of the planar PyDI, indicating a stable charge injection into the CorDI crystal. The electronic conductivity is also attributed to the strong π - π stacking along the bowl-in-bowl and the convex-convex faces in its crystal structure. Similarly, Yin *et al.*¹⁵ designed the bowl-shaped PDI dimers by N-annulation at the bridge sites, which showed enhanced intramolecular charge transport as compared to the dimeric molecule of planar PDIs. Such bowl conformation resulted from the stress strain and the heteroannulation strain along both the N-annulated bay regions.

Besides, bowl-shaped compounds have intriguing optical characteristics that could be beneficial in a variety of optoelectronic applications. As studied by Zhu *et al.*,¹⁶ the heteroatomdoped buckybowl shows excellent optoelectronic property, exhibiting optical absorption in the range of 375-490 nm and green fluorescence in the range of 484-496 nm with high quantum yield. In this case, both UV-vis absorption and fluorescence spectra of

the heteroatom-doped compounds were blue-shifted due to weaker π -conjugation in the molecules as compared to the undoped counterpart. Similarly, Armakovic *et al.*¹⁷ revealed the optical activity of Band N-doped sumanenes in the visible region of solar spectrum. Notwithstanding, only a handful of work on bowl-shaped OSCs are reported in literature. Besides, different functional groups such as halogens and imide were reported to have substantial influences on the optoelectronic and charge transport properties of the organic semiconducting materials.^{18,19} In a recent review article, Haupt and Lentz²⁰ summarized the structure-property relationship in a series of coronene derivatives and inferred that the electron-withdrawing substituents had direct influence on the electron affinity (EA) of the material. Moreover, OSCs functionalized with selective functional groups represent remarkable n-type characteristics. For example, Sanyal *et al.*²¹ investigated the pristine corannulene and its imide functionalized compound; pentafluorophenylcorannulene-5-monoimide, and observed that both possessed n-type semiconducting behavior with the charge mobilities of $\mu_{electron} = 0.1498 \text{ cm}^2\text{V}^{-1}\text{s}^{-1}$ and $\mu_{hole} = 0.0031 \text{ cm}^2\text{V}^{-1}\text{s}^{-1}$. Shi *et al.*²² reported an imide-fused corannulene showing n-type property.

As compared to corannulene and sumanene, the dicyclopenta[ghi, pqr] perylene (DCPP), being a substructure of C_{70} and higher fullerenes, has been less studied due to its synthetic inaccessibility. A single DCPP structure contains one perylene unit with twenty-two sp^2 hybridized carbon atoms, including two five-membered carbon rings fused along the bay positions. Incorporation of these five-membered carbon rings develop global anti-aromaticity that forces the molecule to become diradicaloid by retrieving the aromaticity of the perylene core. This problem has been solved by crowding the side carbon atoms of the cyclopenta ring with the bulky chains. Zou *et al.*²³ have reported the synthesis of aryl-substituted dicyclopenta-[4,3,2,1-ghi:4',3',2',1'-pqr]perylenes, which carries a paratropic current through the outer ring, consequently showing a global antiaromatic behavior. However, the dicationic and dianionic counterparts show aromatic behavior, which is verified from the NICS(1)_{zz} calculations. Alongside, the DFT calculation also revealed a low BWBI barrier ($6.07 \text{ kcal mol}^{-1}$) for the DCPP core, thereby recognizing the advantages of DCPP over the other bowl-shaped structures. Recently, Gao *et al.*²⁴ have demonstrated the BWBI structures of meta substituted diindeno [4,3,2,1-fghi:4',3',2',1'-opqr] perylene (DIP) compounds, out of which the triethylsilyl-ethynyl (TES) functionalized DIP showed p-type characteristics with the mobility value reaching to $0.31 \text{ cm}^2\text{V}^{-1}\text{s}^{-1}$. Whereas, this compound exhibited ambipolar charge transfer characteristics after co-crystallization with C_{70} fullerene

(mobility of hole: $0.40 \text{ cm}^2\text{V}^{-1}\text{s}^{-1}$ and electron: $0.07 \text{ cm}^2\text{V}^{-1}\text{s}^{-1}$), which was further validated from the electronic coupling between the two fragments.

In this work, we present the tuning of hole-to-electron-transporting and ambipolar activity in DCPD-based OSCs through carefully designing their molecular structures. These modelled compounds are roughly classified into three groups as illustrated in **Fig. 1**. Additionally, TES-groups are added to the molecules, concerning their solubility and stability in the operational environment. The structure-property relationship of these DCPD-derivatives is estimated through density functional theory (DFT). Their hypothetical crystal structures are also predicted to estimate the molecular packing arrangements in solid-state. Several factors, such as molecular orbitals, aromaticity, reorganization energies, packing motifs, electronic coupling etc. are taken into consideration when analyzing the charge transport properties of the DCPD-derivatives. The effect of structural changes on non-linear optical behavior of the designed compounds are also investigated.

2. Theory and computational details

The optimal functioning of optoelectronic devices based on OSCs is concomitantly aided by efficient charge injection and high mobility of charge carriers. At room temperature, the incoherent hopping model proposed by the Marcus–Hush equation is used to estimate the charge transfer process of π -conjugated organic semiconductors.^{25–27} The charge hopping rate (K) using the non-adiabatic Marcus theory is described as follows.

$$K = \frac{V_{ij}}{\hbar} \left(\frac{\pi}{\lambda K_B T} \right)^{\frac{1}{2}} \exp \left(- \frac{(\Delta G_{ij} - \lambda)^2}{4 \lambda K_B T} \right) \quad [1]$$

Where \hbar , λ , K_B and T represent the reduced Plank's constant, reorganization energy, Boltzmann constant, and absolute temperature respectively. V_{ij} and ΔG_{ij} are the charge transfer integral and Gibbs free energy difference between the initial and final states, respectively. However, ΔG_{ij} goes off to zero in case of self-exchange reactions, making the Marcus-Hush expression free from the ΔG term.

The following formula can be used to calculate the reorganization energy (λ) using Nelsen's four-point technique.

$$\lambda_{h/e} = (E_{+/-}^* - E_{+/-}) + (E_{h/e}^* - E) \quad [2]$$

Where, $\lambda_{h/e}$ refer to the hole/electron reorganization energies respectively. $E_{+/-}^*$, $E_{+/-}$, $E_{h/e}^*$ and E correspond to the energies of charged states in the neutral geometry, charged states in their own relaxed geometries, neutral states in the geometries of cation/anion species, and ground-state energy of the neutral species respectively. Here, we have considered only the

internal reorganization energy as the external contribution, which is due to the repolarization of surrounding medium is negligible as compared to the internal geometrical relaxation. Based on the molecular orbitals of the conjugated organic materials, the charge transfer integral/ electron coupling (V_{ij}) with respect to different molecular orbitals of the OSC can be calculated by the formula:

$$V_{ij} = \left| \frac{J_{ij} - \frac{1}{2}S_{ij}(e_i + e_j)}{1 - S_{ij}^2} \right| \quad [3]$$

Where, e_i and e_j are the site energies of the i^{th} and j^{th} molecules, mathematically expressed as: $e_{i/j} = \langle \psi_{i/j} | \hat{H} | \psi_{i/j} \rangle$. For a dimer consisting of two nearest neighboring molecules, the charge transfer integrals (J_{ij}) and spatial overlap (S_{ij}) matrix elements can be written as; $J_{ij} = \langle \psi_i | \hat{H} | \psi_j \rangle$ and $S_{ij} = \langle \psi_i | \psi_j \rangle$ respectively, \hat{H} being the Kohn-Sham Hamiltonian of that particular dimer, and the states $\psi_{i/j}$ correspond to the HOMO/LUMO (for hole/electron transport respectively) of the isolated dimers i and j .²⁸

After determining the charge transfer rate, the Einstein-Smoluchowski relation can be used to calculate the charge-hopping mobilities (μ) in the zero-field limit as depicted in the equation below.

$$\mu = \frac{eD}{k_B T} \quad [4]$$

Here, e and D are the electronic charge and diffusion coefficient of the charge carriers (hole/electron) respectively.

The charge transport in an organic crystal with columnar packing is almost one-dimensional. As a result, the diffusion coefficient (D) of charge carriers has a straightforward relationship with K as follows.

$$D = \frac{1}{2} r^2 K \quad [5]$$

Where, r is the intermolecular distance of the dimer under consideration²⁹.

Two molecular descriptors are often employed to evaluate the effectiveness of the process of charge injection from an electrode to an OSC. First is the HOMO and LUMO energy alignment w.r.t the work function (ϕ) of the metal electrode, and secondly, the ionization potential (IP) and electron affinity (EA) of the organic molecules. The metal–semiconductor interface being commonly described as a Mott–Schottky barrier, decides the charge injection process, where the barrier height can be determined by the difference between ϕ and the HOMO/LUMO energy of the OSC. Contrarily, IP and EA of OSC are also the important characteristics for predicting the effectiveness of charge injection from the

electrodes, as well as the oxidation and reduction process upon exposed to air. The adiabatic/vertical electron affinities (AEAs/VEAs) and ionization potentials (AIP/VIP) of the OSCs can be evaluated as;

$$\text{AIP(VIP)} = E_+(E_+^*) - E \quad [6]$$

$$\text{AEA(VEA)} = E - E_-(E_-^*) \quad [7]$$

We use the exchange-correlation hybrid functionals including B3LYP, and PBE0; and dispersion corrected functionals such as B3LYP-D3, and B3LYP-D3(BJ) within the framework of density functional theory (DFT), for optimizing the initial geometries of the molecules. The 6-311G(d,p) triple zeta basis set was used for all the calculations, which is considered as a suitable basis set in balancing the accuracy and computational cost.^{30,31} To ensure whether the molecules have reached their real local minima on the potential energy (PE) surface, the vibrational frequencies are calculated. The absence of imaginary frequencies supports the fact that the molecules have reached their stable equilibria.^{32,33} The charge reorganization energies are computed using four-point method on the adiabatic PE surface with the above mentioned DFT formalism. Furthermore, the electronic structure parameters such as frontier molecular orbitals (FMOs), adiabatic/vertical electron affinities (AEAs/VEAs) and ionization potentials (AIP/VIP) are calculated in the similar fashion. All the calculations have been performed on Gaussian 09 (E.01) package,³⁴ except that, the charge transfer integrals (V_h/V_e) along different hopping channels are computed on the Amsterdam Density Functional (ADF) package with PW91/TZP level of theory.^{35–37} The UV-visible absorption patterns of the DCPD compounds have been simulated in the TD-DFT formalism using polarizable continuum model (PCM), employing TD-CAM-B3LYP/6-311G(d,p) level of theory.^{38,39} We considered twenty states of charge transition in the dichloromethane solvent for this calculation.

3. Results and discussion

3.1. Geometrical analysis

A series of 24 bowl-shaped structures, as shown in **Fig. 1** are designed by taking DCPD as the initial geometry. The designing of these structures was inspired from the report of Huang *et. al.*,⁴⁰ where they have demonstrated the synthesis and optical properties of p-trifluoromethylphenyl (TFMP) substituted DCPD-derivatives. The geometrical information of these compounds (DCPD-TEMP-1, 2, and 3) are obtained from the Cambridge crystallographic data centre (CCDC # 1886505, 1886506, 1886507). These structures are further relaxed using the aforesaid computational methodologies (**Table S1** of the supporting

information). By comparing the geometrical and electronic properties of the optimized structures with the available experimental data, it is found that the B3LYP/6-311G(d,p) method is more suitable in terms of accuracy and computational cost. Therefore, we employed B3LYP/6-311G(d,p) for the study of the other compounds in this series (**Table S2, S3**). Keeping in mind that the bulky TFMP groups in the bay-positions of DCP-TEMPs hinder the intermolecular charge transport, we replaced these groups with hydrogen atoms in our designed structures. As a result, the DCP-1 takes a bowl-shape in contrast to the planar geometry of the experimentally available DCP-TEMP-1 counterpart. Further, the structures of DCP-2 and DCP-3 are obtained by fusing indeno-groups at the peri positions of DCP-1. Also, we performed the end functionalization in DCP-3 by fluorination or imidation to arrive at DCP-4 and 5 respectively (Group-I in **Fig. 1**), whereas, DCP-6, 7 and 8 are designed by aza-substitution at the bay-positions of DCP-3, 4, and 5 respectively (Group-II). DCP-9 to 12 (Group-III) are similarly constructed by integrating hexagonal rings at the ortho-positions of the respective DCP-structures, as shown in **Fig. 1** and **Table S2**. Also, to ensure solubility and stability of the DCP compounds, the triethylsilylethynyl (TES) groups are substituted at the meta positions. This substitution may influence the geometry, aromaticity, electronic structures and crystal packing motifs of DCP-derivatives,^{1,41} which will be explored in the succeeding sections.

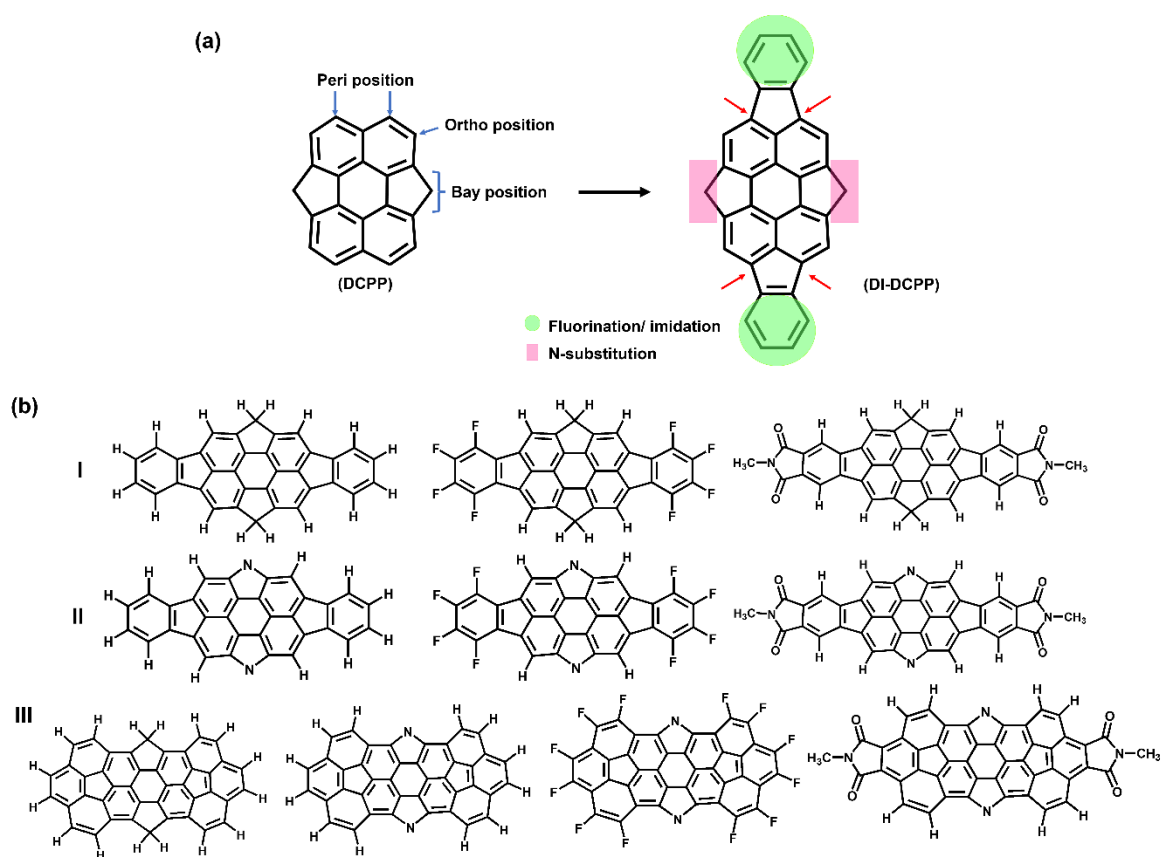


Figure 1. Schematic representation of (a) molecular engineering of DCPD-derivatives, (b) classification of the molecules into three groups; pure, fluoride- and imide-substituted diindeno-DCPDs represented as group-I, their aza-substituted counterparts (group-II), and DCPD-derivatives with ring-annulation at the ortho positions (group-III).

The structural deviation of these bowl-shaped DCPD derivatives can be quantified from the bowl-depth; D_{LS} and cone angle; $\alpha = 2\text{tan}^{-1} \left\{ \frac{(R - r)}{D_{LS}} \right\}$ as reported by Roch *et al.*,² where, r and R are the radii of the circles associated with two extreme centroids, i.e., base and top of the molecular bowls. The bowl-depths and cone angles of the corresponding DCPDs and DCPD-TESs are listed in Table S4. The D_{LS} values undoubtedly increased with the structural changes from DCPD-1 to 5, moreover the aza-substituted DCPDs (group-II) possess higher D_{LS} values as compared to the undoped molecules. The shapes of group-III molecular bowls are quite different from the group-I and II compounds with higher D_{LS} . The α -values were found to decrease with increasing curvature of the molecules. It is also evident that, except DCPD-7, the other compounds do not undergo any significant structural change upon TES-substitution.

3.2. Bowl-to-bowl inversion barrier

3.3. Aromaticity of the DCPD derivatives (NICS1zz and ACID plot)

3.4. Frontier molecular orbitals (FMOs)

The ease of charge injection and air-stability are essential factors for the practical applications of all high-performance OSCs. Therefore, determining the energy levels of FMOs (HOMO and LUMO) is important in estimating the type of materials and their charge injection barriers. The LUMO energy onset for stable electron injection in n-type OSCs is estimated to be -4.0 eV to -4.1 eV.^{42,43} However, OSCs with excessively low LUMO energy may create chemical instability in the air. Hence, with reference to the calcium ($\phi = 2.87$ eV to 2.90 eV), magnesium ($\phi = 3.68$ eV) and gold ($\phi = 5.1$ eV) electrodes, which are the best choices for n-type OSCs, the LUMO levels of the organic materials are reported to be in the range of -3.0 eV to -4.4 eV.^{44,45} Notwithstanding, there exist few reports on the airstable n-type organic materials possessing LUMO level as low as -4.3 eV (in few naphthalene diimide derivatives),⁴⁶ -4.6 eV (for cyano-substituted perylene diimides),^{47,48} -4.9 eV (for fluorinated copper phthalocyanines; F₁₆CuPC)^{42,49,50} etc. Based on the above evidences, we considered the LUMO for air-stable electron injection to be in the range of -4.0 eV to -4.9 eV. As observed in DCP-1, 2 and 3 (**Fig. 2(a)** and **Table S4**), after indeno-substitutions in the bare DCP, the LUMO levels are gradually shifted from -1.919 eV to -2.661 eV. With fluorination (DCP-4) and imidation (DCP-5) at the ends of DCP-3, the LUMO levels are further shifted to -3.267 eV and -3.408 eV respectively. This is due to the electron withdrawing capability of F- and imide-groups in the OSCs. We also observed a similar trend in the aza-substituted compounds (DCP-6, 7 and 8), where the LUMO levels are down-shifted significantly as compared to their undoped counterparts (DCP-3, 4 and 5 respectively). The HOMO and LUMO alignments of DCP-9 differ slightly from those of DCP-3, resulting in a wider HOMO-LUMO gap. This demonstrates that, although ring fusion at the ortho-positions of DCP-3 has no substantial effect on its LUMO level, it does improve its stability. Therefore, we moved further with aza-substitution (DCP-10) and subsequent fluorination and imidation (DCP-11 and 12 respectively) in the structure of DCP-9. After the N-substitution, we observe a significant lowering of LUMO level in DCP-10, as represented in **Fig. 2(a)**. However, after further functionalization, the LUMO levels were shifted much lower, and it is remarkably lower in DCP-11 (-5.157 eV). Such a low-lying LUMO level in DCP-11 is regarded to be unsuitable for OSCs due to chemical instability. DCP-11 was also found to possess the lowest HOMO-LUMO gap (1.413 eV) as compared to the other molecules in the series, where the E_g varied from 1.4-3.1 eV. While comparing the E_g values of group-I, II and III compounds, it is found that the aza-substituted DCPs (group-II) possess lower E_g as compared to group-I molecules. There is a further

decrease of E_g with extending π -conjugation in group-III molecules. A similar trend is also followed by the TES-substituted DCPs (DCPP-TES-1 to 12) as shown in [Fig. 2\(b\)](#) and [Table S4](#).

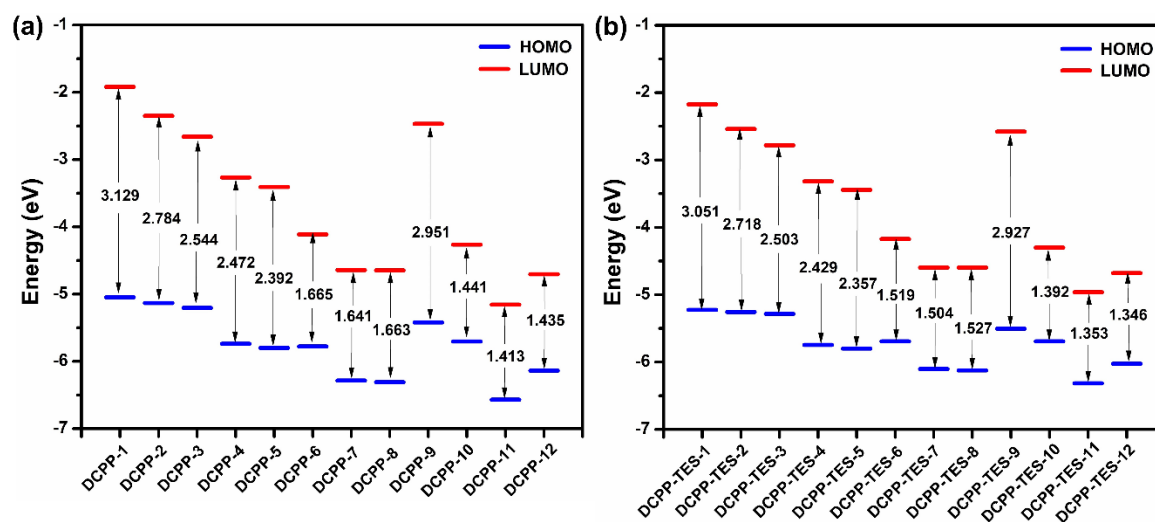


Figure 2. HOMO, LUMO energy levels and HOMO-LUMO gaps of (a) DCP and (b) DCP-TES derivatives.

The spatial distribution of HOMO and LUMO orbitals over the DCPs and the DCP-TES-molecules are presented in [Table S5](#) and [S6](#) respectively. In DCP-1 o 5 it is seen that, both HOMO and LUMO orbitals are delocalized over the entire molecular backbone, indicating the better charge coupling with the neighboring molecules in the crystal. However, after the aza-substitution, the LUMOs are more localized on the DCP core, which may be the consequence of the electron withdrawing property of N-dopants. After the ring fusion at the ortho-positions of DCP compounds, the delocalization of the molecular orbitals is apparently visible, which are emerged from π -conjugation in the systems. Similarly, in some DCP-TES derivatives, we could find the delocalized molecular orbitals along the side chains also. Thus, the TES-substitution may favor the inter-molecular charge transfer in the organic crystal.

3.5. IP, EA and reorganization energy

The hole and electron injection properties of an OSC (p-type/n-type) can be related to the IP (the amount of energy it takes to remove an electron in gas-phase) and EA (the amount of energy liberated when one electron is added to a molecule in gas-phase) values of their monomers. The adiabatic/vertical IP and EA (AIP/VIP and AEA/VEA) of the DCPs and DCP-TESs are listed in [Table 1](#). It is widely believed that the EA should be at least 3.0 eV to allow for facile electron injection to OSC, but no higher than 4.0 eV since negative charges

might react with ambient oxidants like water or oxygen. However, the stability can be restrained by the other parameters such as crystal packing and film morphology. Likewise, low IP is necessary for the operation of p-type OSCs⁵¹. For DCPD compounds in group-I (DCPD-1 to 5), the AIP/VIP and AEA/VEA values are found to be in the range of 6.330-6.839 eV/6.396-6.922 eV and 0.618-2.471 eV/0.511-2.340 eV respectively. Here, the IP values are lowered with the indeno-substitution and then increased with the peripheral F-doping or imide-annulation. However, the EA values gradually increased with indeno- and subsequent peripheral substitutions, favoring electron injection in the modified compounds. After N-doping in the bay-positions of the DCPD bowls (group-II: DCPD-6 to 8), the EA values increased significantly, which are exceeding 3 eV (see [Table 1](#)). Such high EA values would improve the air-stable electron injection ability of the compounds. As we incorporate more number of rings at the ortho-positions of DCPDs (group-III: DCPD-9 to 12), the EA values of the respective compounds are increased. This indicates the fact that the electron injection is more favored with enhancing π -conjugation. For TES-substituted DCPDs, a similar trend was also followed in the IP and EA values. However, we must be aware that DCPD-11 and DCPD-TES-11 have AEA values > 4 eV, which indicates that their stability may be compromised.

Conversely, the charge transporting capacity of an OSC depends on the reorganization energies (λ_h/λ_e : hole/electron reorganization energies), which are dominated by its structural and electronic characteristics. Among the various factors, the longer π -conjugated chain, non-bonding FMOs, and molecular rigidity are significant in lowering λ_h/λ_e which is insisted by the Marcus theory (Eq.1) for getting favorable charge transport in the OSC.^{52,53} Also, lower λ_e improves the electron-transporting ability of the material, which is desirable in our study. The as calculated λ_h and λ_e values of the DCPD-derivatives are presented in [Table 1](#). Out of these, DCPD-TES-10, 11, 12 possess low λ_e as compared to λ_h , suggesting electron-transporting nature of the compounds upon TES substitution in the parent molecules. However, we got equal values of λ_h and λ_e in DCPD-TES-9 (183.92 meV), which designates the fact that DCPD-TES-9 molecule is favorable in both hole- and electron-transportation. When compared the reorganization energies of DCPD-10, it is found that, there is a close association between λ_e (331.81 meV) and λ_h (326.93 meV). The charge transport characteristics of the aforementioned DCPD-derivatives can be further verified from their transfer integrals (V), which are to be discussed in the following section.

Table 1. Internal reorganization energies (λ_h and λ_e), adiabatic and vertical ionization potentials (AIP and VIP) and electron affinities (AEA and VEA) of the DCPD compounds, computed at B3LYP/6-311G(d,p) level of theory.

Compound	AIP (eV)	VIP (eV)	AEA (eV)	VEA (eV)	λ_h (meV)	λ_e (meV)
DCPD-1	6.402	6.473	0.618	0.511	143.70	211.69
DCPD-2	6.358	6.428	1.187	1.068	140.14	237.93
DCPD-3	6.330	6.396	1.599	1.474	133.37	251.17
DCPD-4	6.839	6.922	2.223	2.078	165.74	289.02
DCPD-5	6.837	6.913	2.471	2.340	152.59	262.73
DCPD-6	6.905	7.028	3.054	2.855	273.61	611.41
DCPD-7	7.390	7.524	3.624	3.395	286.22	614.25
DCPD-8	7.364	7.489	3.720	3.481	258.25	611.22
DCPD-9	6.498	6.581	1.427	1.324	167.10	206.11
DCPD-10	6.773	6.895	3.199	3.070	326.93	331.81
DCPD-11	7.565	7.740	4.131	3.975	410.21	379.84
DCPD-12	7.122	7.265	3.743	3.582	384.24	402.05
DCPD-TES-1	6.351	6.443	1.101	0.983	184.92	233.56
DCPD-TES-2	6.305	6.391	1.545	1.421	172.85	245.19
DCPD-TES-3	6.269	6.348	1.853	1.730	159.98	246.99
DCPD-TES-4	6.712	6.802	2.404	2.262	181.07	283.16
DCPD-TES-5	6.717	6.800	2.600	2.472	166.93	256.03
DCPD-TES-6	6.582	6.781	3.296	3.086	266.09	402.05
DCPD-TES-7	6.952	7.175	3.746	3.525	336.00	436.03
DCPD-TES-8	6.943	7.153	3.802	3.580	343.50	450.22
DCPD-TES-9	6.466	6.558	1.640	1.536	183.92	183.92
DCPD-TES-10	6.581	6.746	3.362	3.240	427.67	278.86
DCPD-TES-11	7.144	7.325	4.046	3.914	432.19	327.22
DCPD-TES-12	6.813	7.006	3.841	3.682	393.08	318.23

3.6. Molecular electrostatic potential (ESP) surface analysis

The charge transport properties and molecular packing in an organic crystal depends on the chemical composition and intermolecular interactions. The ESP surface analysis is a qualitative approach of estimating the non-covalent interactions among the molecules in the organic crystal. The structure dependent ESP profiles of DCPDs (Fig. 3) and DCPD-TESs (Fig. S5) are displayed in color spectra. Here, the red and blue regions represent the negative and positive ESP respectively. In DCPD-1, the negative charges are found to be localized on the ring centers, whereas, these are more concentrated on the indeno-positions in DCPD-2 and DCPD-3. However, the electron withdrawing fluorine atoms create positive ESP in DCPD-4, which is apparent from the electron deficient blue regions of DCPD skeleton. It is

believed that, electron delocalization is highly favored by the positive ESP values at the ring centers.⁵⁴ With imide substitution (DCPP-5) also, the core DCPP gets positive ESP, while the negative charges are accumulated on the oxygen atoms of both imide-groups. In aza-substituted compounds (group-II), the negative charges are indeed concentrated at the nitrogen centers, and of course on oxygen atoms of the imide groups of DCPP-8. This trend is also followed by the group-III compounds. The TES-substitution in the DCPPs ([Fig. S5](#)) also maintains similar ESP profiles in their respective compounds.

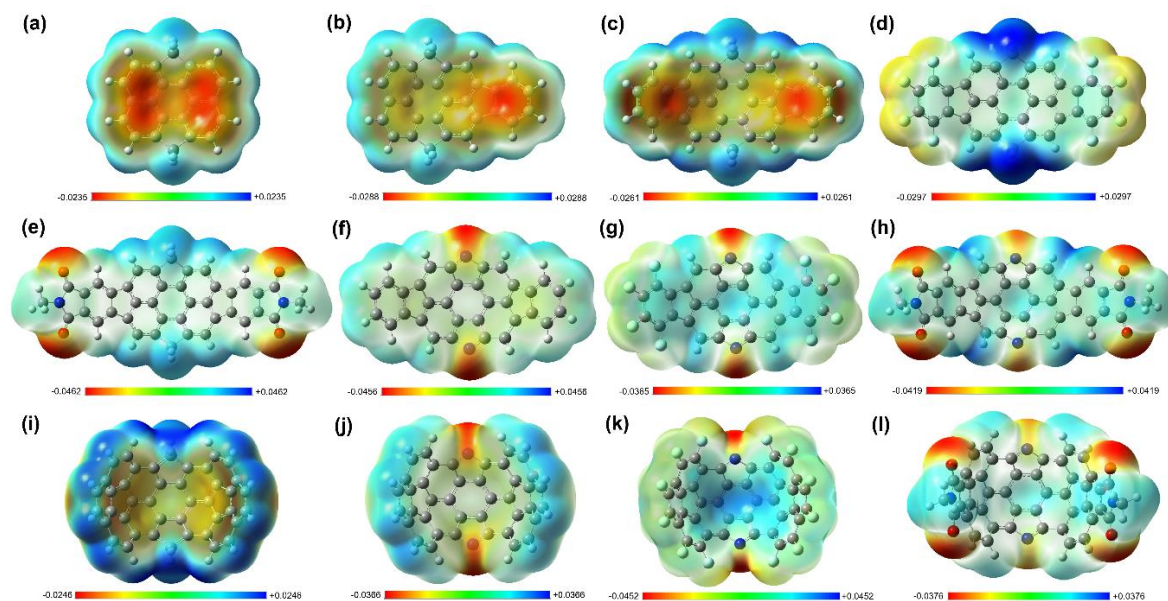


Figure 3. Electrostatic potential (ESP) mapping of the DCPP compounds.

3.7. Crystal structures and charge transfer

Molecular packing motif, being one of the key factors determining the charge transfer parameters are predicted using Materials Studio program as detailed in [Section S1](#) of the supporting information. During the calculation, the geometrical configurations of the molecules are maintained rigid, whereas, only the unit cell parameters are optimized to avoid any molecular deformation. The crystal structures of DCPPs and DCPP-TESs showing different hopping pathways, and their corresponding lattice parameters are presented in [Table S8](#) and [S9](#) respectively. It is evident that all the compounds are packed in either monoclinic or orthorhombic space groups. In terms of their molecular packing, except for DCPP-2, the other DCPP-compounds in group-I are packed into bowl-in-bowl columnar packing with anti-parallel orientation, which is also followed by DCPP-TES-3 and 4. All the group-II compounds and their TES-structures, except the DCPP-TES-8 follow a similar kind

of bowl-in-bowl columnar packing. Also, the deep-bowls of group-III DCPs follow the same trend, which is an exception in DCP-9. For both DCP-9 and DCP-TES-9, we could find the staggered orientation of molecular bowls, and the consecutive dimers are jointly packed in anti-parallel columnar stacking. Both DCP-TES-5 and 8 crystals are also exhibiting stagger-like packing with high molecular disorder. It is considered that the columnar crystal packing of bowl-shaped organic molecules is beneficial in improving the transportation of charge carriers.⁵⁵

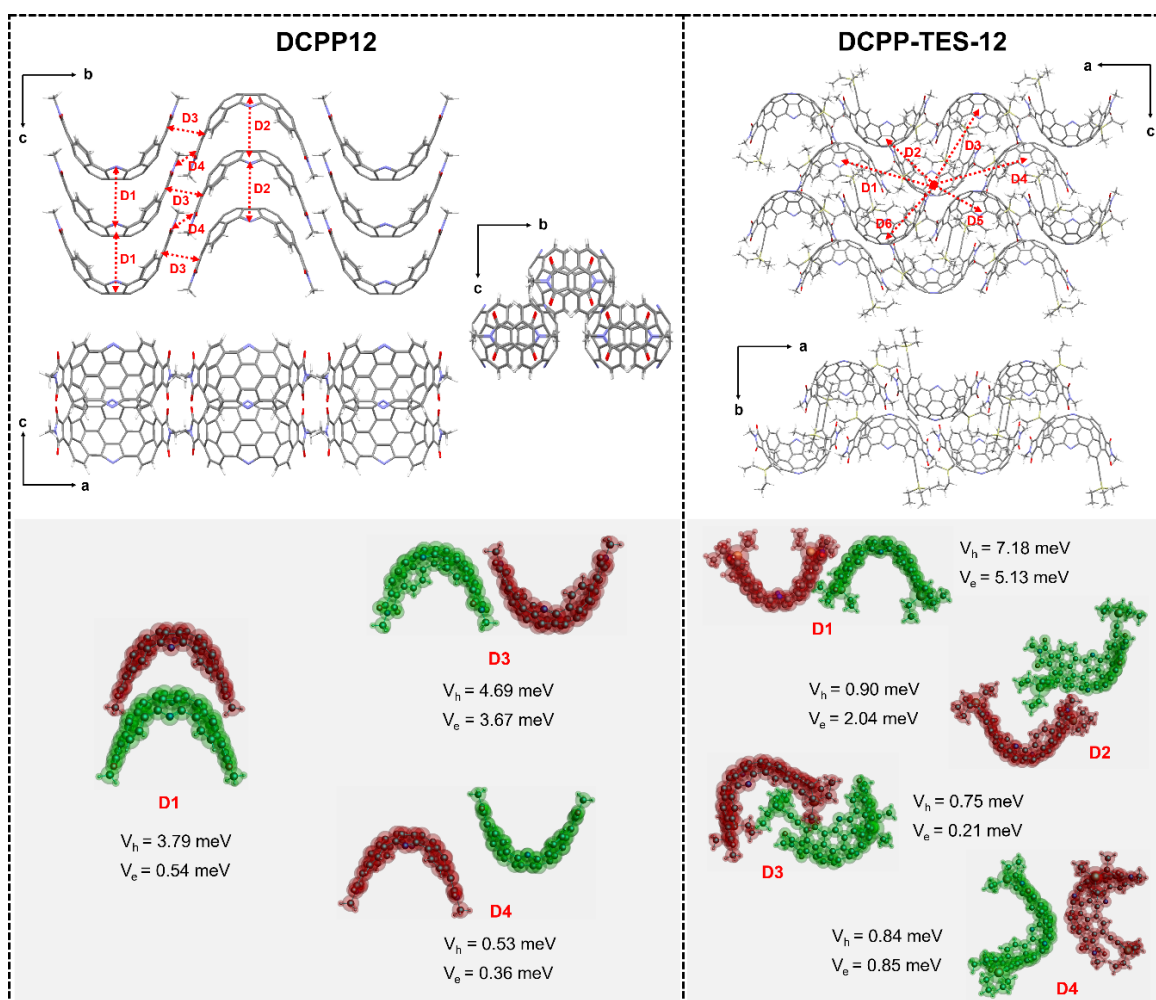


Figure 4. Molecular packing motifs viewed along different planes of the crystals (upper panels), and the intermolecular charge couplings (V_h and V_e) corresponding to the selective dimers (lower panels) of DCP-12 (left panel) and DCP-TES-12 (right panel).

The intermolecular electronic coupling is an important factor in determining the charge transport property of an OSC, that depends on the relative positioning and orientation of the neighboring molecules in the crystal. **Table 2** gathers the charge transport parameters of DCP- and DCP-TES-derivatives: hopping pathways, intermolecular distances (r), the

corresponding hole/electron couplings (V_h/V_e), hole/electron transfer rates (K_h/K_e), and diffusion mobilities for holes/electrons (μ_h/μ_e). The hopping pathways D1, D2, D3, ... are presented by the dotted red-lines in the crystal structures of the studied compounds (see **Fig. 4** and **Fig S3-S26**). The electronic couplings of these DCPD-based structures as calculated using ADF: PW91/TZP level were found to be as high as ~85 meV (for V_h) and ~78 meV (for V_e), which are close to various previously reported figures. For example, the hole transporting characteristics of biphenylene-containing acenes ($V_h=0-50.04$ meV computed at PW91/TZP level)⁵⁶, fluoroarene-oligothiophene ($V_h=26-53$ meV at PW91/TZP level)⁵⁷, aryl-substituted anthracene ($V_h=57$ meV at PW91/TZP level)³⁷, benzothiophenes ($V_h=6.88-69.41$ meV at PW91PW91/ def2-TZVP level)⁵⁸, octaseleno[8]circulene ($V_h= 73.61$ meV at PW91PW91/6-31G(d,p) level)⁵⁹ have been reported. Similarly, the electron couplings of several n-type OSCs are investigated: imide-fused corannulene derivative ($V_e= 2.28-131$ meV at PBE0/DZP level)¹², naphthodithiophene diimide ($V_e= 12.6-120.1$ meV at PW91/TZ2P level)¹⁸, perylene diimide ($V_e= 0-110.29$ meV at PW91PW91/ 6-31G(d))⁶⁰, aza[6]helicene ($V_e= 40-70$ meV at B3LYP/6-31G(d))⁶¹, perfluoropentacene ($V_e= 0-79.36$ meV), TIPS-PENTCN₄ ($V_e= 0-44.61$ meV) calculated at PW91/TZ2P level⁶², and different other OSCs. It is evident from the obtained results that the intermolecular charge coupling is stronger in the DCPDs and DCPD-TESs with bowl-in-bowl concave-convex packing and stacking along convex-convex faces.

Once the information on V_h/V_e and λ_h/λ_e are obtained, the charge transfer integrals for holes and electrons can be computed using Eq. 1. The calculated values of K_h and K_e as presented in **Table 2** suggest that DCPD-TES-1 has the highest K_h ($= 4.70 \times 10^{13} \text{ s}^{-1}$) for hole hopping among the other compounds. Nevertheless, the K_h for DCPD-9 and DCPD-TES-4 are found to be in the same order (i.e., 10^{13} s^{-1}). Besides, DCPD-1, DCPD-2, DCPD-3, DCPD-TES-2 and DCPD-TES-3, which are particularly well suited for hole injection, also have K_h values in the range of $10^{11}-10^{12} \text{ s}^{-1}$, signifying the hole transporting ability of these compounds. When the electron transfer rates of DCPD-derivatives are compared, the maximum K_e for the compounds showing favorable electron injection character (DCPD-6, 7, 8, 10, 12, and the TES-analogues) are found in the order of $10^8-10^{12} \text{ s}^{-1}$. However, the DCPD-TES-derivatives (DCPD-TES-6, 7, 8 and 10) reveal higher K_e value as compared to K_h , which supports the n-type characteristics in the materials. Furthermore, we observed a balanced hole and electron transport found in DCPD-12 and DCPD-TES-12, which may result in the ambipolar characteristics in the material. The charge transport properties of the DCPD-

derivatives are finally validated by their charge carrier mobilities, which are determined using Eq. 4. The p-type characteristics are found in DCP-1, 2, 3, their TES-derivatives, and DCP-9 with appropriate hole injection as well as hole transport behavior. The hole mobility of DCP-9 ($\mu_h = 6.296 \text{ cm}^2\text{V}^{-1}\text{s}^{-1}$) is found to be the highest in the series. Similarly, the highest $\mu_e = 0.142 \text{ cm}^2\text{V}^{-1}\text{s}^{-1}$ was discovered in DCP-TES-6, which is better than many reported values in bowl-shaped OSCs.^{12,14,22} The electron-mobilities of DCP-TES-7, 8 and 10 are found to be 1.40×10^{-3} , 3.36×10^{-5} and $4.27 \times 10^{-2} \text{ cm}^2\text{V}^{-1}\text{s}^{-1}$ respectively, revealing the ability of N-doping to induce n-type characteristic in these OSCs. On the other hand, both DCP-12 ($\mu_h / \mu_e = 4.90 \times 10^{-3} / 2.50 \times 10^{-3} \text{ cm}^2\text{V}^{-1}\text{s}^{-1}$) and DCP-TES-12 ($\mu_h / \mu_e = 1.04 \times 10^{-2} / 1.22 \times 10^{-2} \text{ cm}^2\text{V}^{-1}\text{s}^{-1}$) exhibit balanced hole and electron mobilities, where, the mobility is enhanced by one order of magnitude after TES-substitution. Hence, the charge mobility of DCP-based compounds can be tuned from unipolar (p-type or n-type) to ambipolar by using appropriate molecular designing techniques and formulations.

Table 2. Computed values of charge transport parameters of the DCP- and DCP-TES-derivatives: intermolecular distances (r) along different hopping pathways, intermolecular hole/electron couplings (V_h/V_e), hole/electron transfer rates (K_h/K_e), and diffusion mobilities for hole/electron (μ_h/μ_e).

Compound	Pathways	r (Å)	$ V_h $ (meV)	$ V_e $ (meV)	K_h (s ⁻¹)	K_e (s ⁻¹)	μ_h (cm ² V ⁻¹ s ⁻¹)	μ_e (cm ² V ⁻¹ s ⁻¹)	μ_h^{\max} (cm ² V ⁻¹ s ⁻¹)	μ_e^{\max} (cm ² V ⁻¹ s ⁻¹)
DCPP-1	D1, D2	3.669	3.80	77.96	1.57×10^{11}	2.82×10^{13}	4.10×10^{-3}	0.738	2.04×10^{-2}	0.738
	D3	10.788	5.51	9.35	3.31×10^{11}	4.05×10^{11}	7.50×10^{-2}	9.18×10^{-2}		
	D4	10.992	2.82	0.89	8.67×10^{10}	3.67×10^9	2.04×10^{-2}	8.63×10^{-4}		
DCPP-2	D1, D2	3.904	26.25	32.27	7.92×10^{12}	3.54×10^{12}	0.235	0.105	0.409	0.301
	D3, D5	10.883	0.58	2.65	3.87×10^9	2.38×10^{10}	8.92×10^{-4}	5.50×10^{-3}		
	D4	11.328	11.94	18.84	1.64×10^{12}	1.21×10^{12}	0.409	0.301		
	D6	10.085	2.78	1.98	8.88×10^{10}	1.33×10^{10}	1.76×10^{-2}	2.60×10^{-3}		
DCPP-3	D7, D8	14.513	3.60	5.48	1.49×10^{11}	1.02×10^{11}	6.11×10^{-2}	4.18×10^{-2}	0.167	2.41×10^{-2}
	D1, D2	4.015	9.27	0.52	1.08×10^{12}	7.88×10^8	3.40×10^{-2}	2.47×10^{-5}		
	D3	11.309	6.67	3.07	5.62×10^{11}	2.75×10^{10}	0.140	6.80×10^{-3}		
	D4	11.602	0.02	0.38	5.05×10^6	4.21×10^8	1.32×10^{-6}	1.10×10^{-4}		
	D5	17.184	2.50	3.79	7.89×10^{10}	4.18×10^{10}	4.54×10^{-2}	2.41×10^{-2}		
DCPP-4	D1, D2	4.047	25.31	21.04	5.25×10^{12}	8.30×10^{11}	0.167	2.65×10^{-2}	0.167	2.65×10^{-2}
	D3	12.184	0.75	1.19	4.61×10^9	2.66×10^9	1.30×10^{-3}	7.68×10^{-4}		
	D4	11.617	1.48	7.02	1.79×10^{10}	9.24×10^{10}	4.70×10^{-3}	2.43×10^{-2}		
	D5	17.992	0.97	0.85	7.71×10^9	1.35×10^9	4.90×10^{-3}	8.54×10^{-4}		
DCPP-5	D1, D2	4.090	15.57	7.28	2.35×10^{12}	1.34×10^{11}	7.65×10^{-2}	4.40×10^{-3}	0.016	0.225
	D3	14.066	2.04	15.20	4.03×10^{10}	5.85×10^{11}	0.016	0.225		
	D4	14.353	0.88	0.58	7.50×10^9	8.52×10^8	0.003	3.42×10^{-4}		
	D5	24.516	0	0	0	0	0	0		
DCPP-6	D1, D2	4.268	63.80	45.58	9.07×10^{12}	1.17×10^{11}	0.322	0.004	0.322	0.004
	D3	11.734	0.26	1.31	1.51×10^8	9.63×10^7	4.04×10^{-5}	2.58×10^{-5}		
	D4	12.351	1.25	0.01	3.48×10^9	5.61×10^3	0.001	1.67×10^{-9}		
	D5	15.812	1.99	1.08	8.83×10^9	6.55×10^7	4.30×10^{-3}	3.19×10^{-5}		
DCPP-7	D1, D2	4.240	4.49	6.82	3.91×10^{10}	2.53×10^9	1.40×10^{-3}	8.85×10^{-5}	0.145	2.05×10^{-4}
	D3	12.204	0.90	0.33	1.57×10^6	5.92×10^6	4.56×10^{-4}	1.72×10^{-6}		

DCPP-8	D4	11.883	16.48	3.70	5.27×10^8	7.44×10^8	0.145	2.05×10^{-4}	0.106	2.31×10^{-4}
	D1, D2	4.399	32.37	10.46	2.81×10^{12}	6.14×10^9	0.106	2.31×10^{-4}		
	D3	13.181	0.88	2.11	2.08×10^9	2.50×10^8	7.03×10^{-4}	8.45×10^{-5}		
DCPP-9	D4	13.622	0.73	0.52	1.43×10^9	1.52×10^7	5.17×10^{-4}	5.48×10^{-6}	6.296	3.050
	D1, D2	6.264	3.72	19.44	1.12×10^{11}	1.88×10^{12}	8.60×10^{-3}	0.144		
	D3	13.084	0	0.09	0	4.03×10^7	0	1.35×10^{-5}		
DCPP-10	D4	10.279	61.50	54.54	3.06×10^{13}	1.48×10^{13}	6.296	3.050	3.36×10^{-2}	1.75×10^{-2}
	D5, D6	8.873	3.72	14.76	1.12×10^{11}	1.09×10^{12}	1.72×10^{-2}	0.166		
	D1, D2	10.388	9.84	5.97	1.18×10^{11}	4.10×10^{10}	2.48×10^{-2}	8.60×10^{-3}		
DCPP-11	D3	10.781	11.04	4.06	1.48×10^{11}	1.90×10^{10}	3.36×10^{-2}	4.30×10^{-3}	0.59×10^{-2}	8.10×10^{-3}
	D4	7.658	8.84	11.53	9.52×10^{10}	1.53×10^{11}	1.09×10^{-2}	1.75×10^{-2}		
	D1, D2	10.798	3.77	7.29	6.89×10^9	3.58×10^{10}	1.60×10^{-3}	8.10×10^{-3}		
DCPP-12	D3	11.205	7.07	1.33	2.42×10^{10}	1.19×10^9	0.59×10^{-2}	2.92×10^{-4}	4.90×10^{-3}	2.50×10^{-3}
	D4	8.245	2.15	3.83	2.24×10^9	9.89×10^9	2.97×10^{-4}	1.30×10^{-3}		
	D1, D2	7.831	3.79	0.54	9.27×10^9	1.54×10^{10}	1.10×10^{-3}	1.80×10^{-3}		
DCPP-TES-1	D3	13.298	4.69	3.67	1.42×10^{10}	7.13×10^9	4.90×10^{-3}	2.50×10^{-3}	1.810	0.476
	D4	15.915	0.53	0.36	1.81×10^8	6.86×10^7	8.94×10^{-5}	3.38×10^{-5}		
	D1, D5	21.026	0.03	0.03	5.81×10^6	3.20×10^6	5.00×10^{-6}	2.76×10^{-6}		
DCPP-TES-2	D2, D8	20.629	0.03	0.07	5.81×10^6	1.75×10^7	4.81×10^{-6}	1.45×10^{-5}	8.70×10^{-3}	9.22×10^{-2}
	D3, D7	4.447	85.36	58.90	4.70×10^{13}	1.24×10^{13}	1.810	0.476		
	D4, D6	22.321	0	0	0	0	0	0		
DCPP-TES-3	D1, D5	18.541	0.01	0	7.50×10^5	0	5.02×10^{-7}	0	0.217	0.125
	D2, D8	18.867	0.08	0.05	4.80×10^7	7.82×10^6	3.33×10^{-5}	5.42×10^{-6}		
	D3, D7	4.015	6.08	30.66	2.77×10^{11}	2.94×10^{12}	8.70×10^{-3}	9.22×10^{-2}		
DCPP-TES-4	D4, D6	19.074	0.07	0.27	3.67×10^7	2.28×10^8	2.60×10^{-5}	1.61×10^{-4}	6.178	0.776
	D1, D2	4.172	7.59	21.26	5.10×10^{11}	1.38×10^{12}	0.017	0.047		
	D3	16.486	6.81	8.81	4.10×10^{11}	2.37×10^{11}	0.217	0.125		
DCPP-TES-5	D4	17.011	0.59	1.02	3.08×10^9	3.18×10^9	1.70×10^{-3}	1.80×10^{-3}	2.02×10^{-6}	1.96×10^{-5}
	D1, D2	7.600	1.10	0.03	8.21×10^9	1.81×10^6	9.23×10^{-4}	2.03×10^{-7}		
	D3	9.406	25.65	40.44	4.46×10^{12}	3.29×10^{12}	0.769	0.566		
DCPP-TES-5	D4	10.322	66.27	43.15	2.98×10^{13}	3.74×10^{12}	6.178	0.776	2.02×10^{-6}	1.96×10^{-5}
	D5	18.073	1.24	1.05	1.04×10^{10}	2.22×10^9	6.60×10^{-3}	4.60×10^{-4}		
	D1, D2	13.686	0.01	0.04	8.09×10^5	4.40×10^6	2.95×10^{-7}	1.60×10^{-6}		
DCPP-TES-5	D3	14.711	0	0.02	0	1.10×10^6	0	4.63×10^{-7}	2.02×10^{-6}	1.96×10^{-5}
	D4	11.948	0.03	0.16	7.28×10^6	7.03×10^7	2.02×10^{-6}	1.96×10^{-5}		

DCPP-TES-6	D1, D2	9.742	12.05	38.11	3.55×10^{11}	7.69×10^{11}	6.56×10^{-2}	0.142	6.56×10^{-2}	0.142
	D3	12.948	0.01	0.02	2.45×10^5	2.12×10^5	7.98×10^{-8}	6.91×10^{-8}		
	D4, D5	12.372	0.11	1.03	2.96×10^7	5.61×10^8	8.82×10^{-6}	1.67×10^{-4}		
DCPP-TES-7	D1, D2	8.190	0.36	0.89	1.43×10^8	2.89×10^8	1.86×10^{-5}	3.78×10^{-5}	2.52×10^{-4}	1.40×10^{-3}
	D3, D4	9.000	0.84	1.75	7.77×10^8	1.12×10^9	1.22×10^{-4}	1.76×10^{-4}		
	D5, D6	10.537	1.03	4.26	1.17×10^9	6.62×10^9	2.52×10^{-4}	1.40×10^{-3}		
	D7, D8	17.384	0.06	0.01	3.96×10^6	3.65×10^4	2.33×10^{-6}	2.15×10^{-8}		
DCPP-TES-8	D1, D2	21.546	0	0.01	0	3.13×10^4	0	2.83×10^{-8}	1.25×10^{-6}	3.36×10^{-5}
	D3, D4	18.330	0	0	0	0	0	0		
	D5, D6	11.421	0.07	0.65	4.93×10^6	1.32×10^8	1.25×10^{-6}	3.36×10^{-5}		
DCPP-TES-9	D1, D3	10.778	0.90	0.05	5.29×10^9	1.63×10^6	1.20×10^{-3}	3.69×10^{-6}	3.25×10^{-2}	4.52
	D2	15.271	0.23	0.56	3.46×10^8	2.05×10^9	1.57×10^{-4}	9.30×10^{-4}		
	D4	12.028	4.20	49.57	1.15×10^{11}	1.61×10^{13}	3.25×10^{-2}	4.52		
	D5, D6	17.607	0.04	0.46	1.05×10^7	1.38×10^9	6.31×10^{-6}	8.34×10^{-4}		
DCPP-TES-10	D1, D2	13.351	1.40	7.65	7.81×10^8	1.23×10^{11}	2.71×10^{-4}	4.27×10^{-2}	2.70×10^{-3}	4.27×10^{-2}
	D3	10.395	5.64	0.87	1.27×10^{10}	1.59×10^9	2.70×10^{-3}	3.35×10^{-4}		
	D4	12.790	0.17	5.33	1.15×10^7	5.98×10^{10}	3.67×10^{-6}	1.90×10^{-2}		
DCPP-TES-11	D1, D2	15.462	0.07	0.09	1.87×10^6	9.86×10^6	8.70×10^{-7}	4.59×10^{-6}	5.80×10^{-3}	6.30×10^{-2}
	D3, D4	7.910	0.01	4.99	3.81×10^4	3.03×10^{10}	4.64×10^{-9}	3.70×10^{-3}		
	D5, D6	12.975	0.52	3.96	1.03×10^8	1.91×10^{10}	3.38×10^{-5}	6.30×10^{-2}		
	D7, D8	12.881	6.85	2.17	1.79×10^{10}	5.73×10^9	5.80×10^{-3}	1.90×10^{-3}		
DCPP-TES-12	D9, D10	13.872	0.12	0.10	5.49×10^6	1.22×10^7	2.06×10^{-6}	4.56×10^{-6}		
	D1, D4	13.308	7.18	5.13	3.01×10^{10}	3.55×10^{10}	1.04×10^{-2}	1.22×10^{-2}	1.04×10^{-2}	1.22×10^{-2}
	D2, D6	12.063	0.90	2.04	4.73×10^8	5.61×10^9	1.34×10^{-4}	1.60×10^{-3}		
	D3	11.099	0.75	0.21	3.29×10^8	5.95×10^7	7.88×10^{-5}	1.43×10^{-5}		
	D5	13.108	0.84	0.85	4.12×10^8	9.74×10^8	1.38×10^{-4}	2.34×10^{-4}		

3.8. Linear and non-linear optical properties

The photoexcitation properties of the DCPD derivatives are analyzed from the UV-visible absorption spectra as presented in [Fig. 4](#). Here, twenty states are considered to obtain the photoabsorption spectra using the aforementioned method. As evident from [Fig. 4](#), all the studied compounds are optically active and show well-defined high intensity bands in the UV to visible region of the solar spectrum (206-877 nm). These absorption spectra can be roughly divided into three regions, namely, short wavelength (190-300 nm), medium wavelength (300-400 nm) and long wavelength (> 400 nm) regions. The notable absorption wavelengths (λ_{abs}), oscillator strengths (f), excitation energies, and major spectral compositions of the corresponding DCPDs and DCPD-TESs are listed in [Table S9](#) for reference. In DCPD-1 to 5 and their TES-counterparts, the most intense bands are observed in the short wavelength region, however, the intensities of TES-based compounds are found to be enhanced in this range ([Fig. 4\(a, d\)](#)), which is attributed to the extended π -electron delocalization in DCPD-TES structures.⁶³ On the other hand, the bands are found to be broadened in the medium to long wavelength region, indicating the presence of abundant vibrational and rotational sublevels. It is worth noting that, with indeno-substitutions and subsequent fluorination/imidation, the absorption spectra undergo bathochromic shifting, among which the imidized DCPDs (DCPD-5 and DCPD-TES-5) show better optical activity. In DCPD-5 and DCPD-TES-5, the absorption peaks found in the range of 520-530 nm are corresponding to $S_0 \rightarrow S_1$ transitions, originated from the H \rightarrow L electronic transitions ([Table S9](#)). In contrast to the undoped DCPDs, the N-doped DCPDs ([Fig. 4\(b\)](#)) are found to possess high intensity bands in the range of 260-300 nm along with few broad peaks in the mid-wavelengths (< 400 nm). However, the TES-side chains help in shifting the spectra to the higher wavelengths. The distinctive bands could be found near 500 nm in DCPD-TES-6 to 8, which are majorly contributed by H-2 \rightarrow L (~75 %) transitions. As seen in DCPD-9 to 12 and DCPD-TES-9 to 12, the absorption spectra are expanded towards the red region (~ 700 nm) upon structural modification, which is significantly observed in DCPD-TESs. In DCPD-TES-10, 11 and 12, the bands appearing beyond 650 nm are mainly contributed from the H-2 \rightarrow L and H-1 \rightarrow L transitions. As a whole, it can be concluded that the structural modification of DCPD-bowls influences the optical absorption property of the materials.

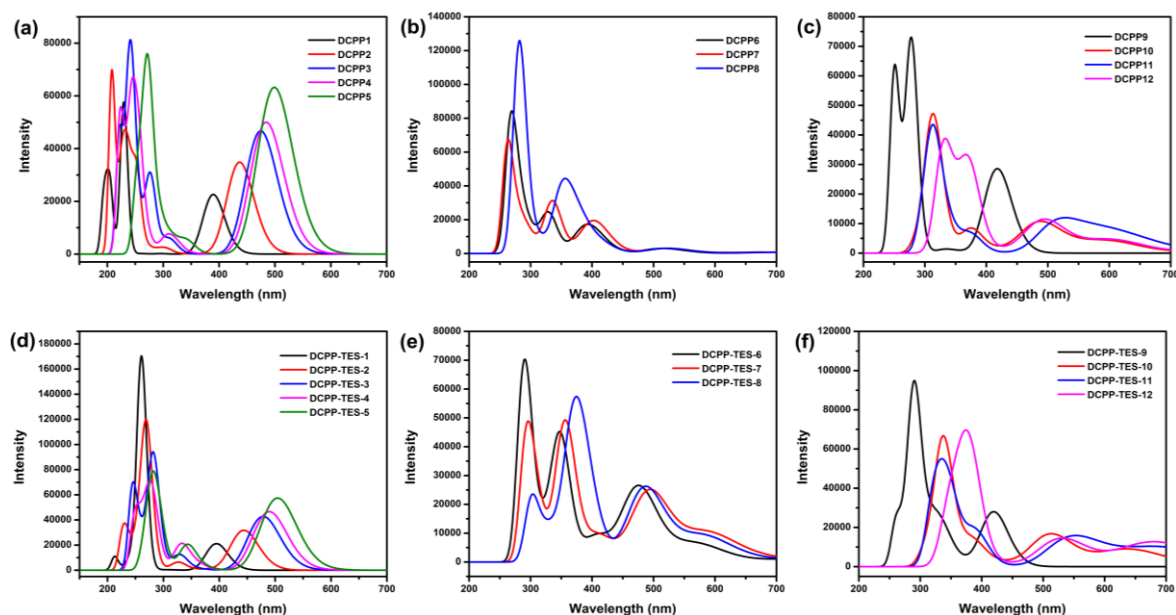


Figure 5. UV-visible absorption spectra of (a-c) DCPP and (d-f) DCPP-TES compounds in dichloromethane solvent simulated with PCM model.

4. Conclusion

To summarize and conclude, we have demonstrated the structure-property relationship of 24 DCPP-based organic compounds, all of which have bowl-shaped molecular features and mostly packed into bowl-in-bowl columnar stacking in the crystal. The electron injection criteria are satisfied by some of the studied compounds including all group-II derivatives; DCPP-10 and 12 in group-III and their TES-analogues. This is confirmed by their low-lying LUMO level (< -4 eV) and high electron affinity (> 3 eV) values, enabling the air-stability of these DCPP-derivatives under ambient operating condition. However, the fluorinated structures in group-III possess ultra-low LUMO levels and EAs > 4 eV, which may compromise their air-stability. Regarding the charge transport characteristics, the DCPP-derivatives are showing unipolar to ambipolar behavior upon structural modification. The highest μ_h and μ_e were found in DCPP-9 ($6.296 \text{ cm}^2\text{V}^{-1}\text{s}^{-1}$) and DCPP-TES-6 ($0.142 \text{ cm}^2\text{V}^{-1}\text{s}^{-1}$) respectively. On the other hand, DCPP-12 and DCPP-TES-12 showed ambipolar charge transport behavior. DCPP-TES-12 in particular enables the enhancement in both μ_h ($1.04 \times 10^{-2} \text{ cm}^2\text{V}^{-1}\text{s}^{-1}$) and μ_e ($1.22 \times 10^{-2} \text{ cm}^2\text{V}^{-1}\text{s}^{-1}$) by ten-times as compared to DCPP-12, making it suitable for ambipolar transistor applications. The DCPP-derivatives are also optically active in the UV-visible region, which is confirmed from the TD-DFT analysis. Inspired from their non-centrosymmetric molecular geometry and optical activity, we also investigated their non-linear optical (NLO) responses, which may pave their way towards applications in photonics and optoelectronics.

Acknowledgement

SD and SS acknowledge Indian Institute of Technology (ISM), Dhanbad for research facilities and financial support. We also acknowledge Prof. B. R. K. Nanda, Department of Physics, IIT Madras and HPCE, IIT Madras for providing the computational facilities.

Supporting Information Available

It contains (a) comparison of DFT methods; (b) optimized geometry of DCPD derivatives; (c) bowl-depth and cone angle of DCPD derivatives; (d) FMO distribution; (e) ESP map of DCPD derivatives; (f) molecular packing motifs; (g) crystallographic information; and (h) Optical absorption details.

References

1. Gao, G.; Chen, M.; Roberts, J.; Feng, M.; Xiao, C.; Zhang, G.; Parkin, S.; Risko, C.; Zhang, L. *J. Am. Chem. Soc.* **2020**, *142*, 2460–2470.
2. Roch, L. M.; Zoppi, L.; Siegel, J. S.; Baldrige, K. K. *J. Phys. Chem. C* **2017**, *121*, 1220–1234.
3. Fu, B.; Hou, X.; Wang, C.; Wang, Y.; Zhang, X.; Li, R.; Shao, X.; Hu, W. *Chem. Commun.* **2017**, *53*, 11407–11409.
4. Pun, S. H.; Wang, Y.; Chu, M.; Chan, C. K.; Li, Y.; Liu, Z.; Miao, Q. *J. Am. Chem. Soc.* **2019**, *141*, 9680–9686.
5. Nestoros, E.; Stuparu, M. C. *Chem. Commun.* **2018**, *54*, 6503–6519.
6. Lovas, F. J.; McMahon, R. J.; Grabow, J.-U.; Schnell, M.; Mack, J.; Scott, L. T.; Kuczkowski, R. L. *J. Am. Chem. Soc.* **2005**, *127*, 4345–4349.
7. Noguchi, Y.; Miyazaki, Y.; Tanaka, Y.; Sato, N.; Nakayama, Y.; Schmidt, T. D.; Brutting, W.; Ishii, H. *J. Appl. Phys.* **2012**, *111*, 114508.
8. Lu, R.-Q.; Wu, S.; Yang, L.-L.; Gao, W.-B.; Qu, H.; Wang, X.-Y.; Chen, J.-B.; Tang, C.; Shi, H.-Y.; Cao, X.-Y. *Angew. Chem. Int. Ed.* **2019**, *58*, 7600–7605.
9. Saito, M.; Shinokubo, H.; Sakurai, H. *Mater. Chem. Front.* **2018**, *2*, 635–661.
10. Ball, M.; Zhong, Y.; Wu, Y.; Schenck, C.; Ng, F.; Steigerwald, M.; Xiao, S.; Nuckolls, C. *Acc. Chem. Res.* **2015**, *48*, 267–276.
11. Karaush, N. N.; Baryshnikov, G. V.; Agren, H.; Minaev, B. F. *New J. Chem.* **2018**, *42*, 11493–11505.
12. Lu, R.-Q.; Liu, Y.; Wu, S.; Saha, M.; Qu, H.; Chen, R.; Yang, L.-L.; Wang, X.-Y.; Wang, Y.; Weng, W.; Zhao, Y.; Cao, X. *Cryst. Growth Des.* **2018**, *18*, 4240–4244.

13. Xu, Q.; Wang, C.; Zheng, D.; He, J.; Wang, Y.; Chen, X.; Jiang, H. *J. Org. Chem.* **2021**, *86*, 13990–13996.
14. Fu, X.; Zhen, Y.; Ni, Z.; Li, Y.; Dong, H.; Siegel, J. S.; Hu, W. *Angew. Chem. Int. Ed.* **2020**, *59*, 14024–14028.
15. Yin, H.; Sui, M.-Y.; Pan, Q.-Q.; Sun, G.-Y.; Geng, Y. *Dyes Pigm.* **2018**, *148*, 394–404.
16. Zhu, G.; Song, Y.; Zhang, Q.; Ding, W.; Chen, X.; Wang, Y.; Zhang, G. *Org. Chem. Front.* **2021**, *8*, 727–735.
17. Armakovic, S.; Armakovic, S. J.; Setrajcic, J. P.; Setrajcic, I. *J. Chem. Phys. Lett.* **2013**, *578*, 156–161.
18. Ji, L.-F.; Fan, J.-X.; Zhang, S.-F.; Ren, A.-M. *Phys. Chem. Chem. Phys.* **2017**, *19*, 13978–13993.
19. Feng, K.; Zhang, X.; Wu, Z.; Shi, Y.; Su, M.; Yang, K.; Wang, Y.; Sun, H.; Min, J.; Zhang, Y.; Cheng, X.; Woo, H. Y.; Guo, X. *ACS Appl. Mater. Interfaces* **2019**, *11*, 35924–35934.
20. Haupt, A.; Lentz, D. *Chem. Eur. J.* **2019**, *25*, 3440–3454.
21. Sanyal, S.; Manna, A. K.; Pati, S. K. *ChemPhysChem* **2014**, *15*, 885–893.
22. Shi, K.; Lei, T.; Wang, X.-Y.; Wang, J.-Y.; Pei, J. *Chem. Sci.* **2014**, *5*, 1041–1045.
23. Zou, Y.; Zeng, W.; Gopalakrishna, T. Y.; Han, Y.; Jiang, Q.; Wu, J. *J. Am. Chem. Soc.* **2019**, *141*, 7266–7270.
24. Gao, G.; Chen, M.; Roberts, J.; Feng, M.; Xiao, C.; Zhang, G.; Parkin, S.; Risko, C.; Zhang, L. *J. Am. Chem. Soc.* **2020**, *142*, 2460–2470.
25. Chen, F.; Wang, Y.; Zhang, W.; Tian, T.; Bai, B.; Wang, H.; Bai, F.-Q.; Li, M. *Cryst. Growth Des.* **2019**, *19*, 6100–6113.
26. Yavuz, I.; Martin, B. N.; Park, J.; Houk, K. N. *J. Am. Chem. Soc.* **2015**, *137*, 2856–2866.
27. Jiang, Y.; Geng, H.; Li, W.; Shuai, Z. *J. Chem. Theory Comput.* **2019**, *15*, 1477–1491.
28. Fan, J.-X.; Ji, L.-F.; Zhang, N.-X.; Lin, P.-P.; Qin, G.-Y.; Zhang, S.-F.; Ren, A.-M. *New J. Chem.* **2019**, *43*, 3583–3600.
29. X. Chen, H. Sakurai, H. Wang, S. Gao, H. -D. Bi, F. -Q. Bai, *Phys. Chem. Chem. Phys.* **2021**, *23*, 4681.
30. Muniz-Miranda, F.; Menziani, M. C.; Pedone, A. *J. Phys. Chem. C* **2014**, *118*, 7532–7544.
31. Wiebeler, C.; Vollbrecht, J.; Neuba, A.; Kitzerow, H.-S.; Schumacher, S. *Sci. Rep* **2021**, *11*, 16097.
32. Hao, M.; Chi, W.; Li, Z. *Chem. Asian J.* **2020**, *15*, 287–293.

33. Yao, C.; Yang, Y.; Li, L.; Bo, M.; Zhang, J.; Peng, C.; Huang, Z.; Wang, J. *J. Phys. Chem. C* **2020**, *124*, 23059–23068.
34. Frisch, M. J. et al. Gaussian09 Revision E.01. Gaussian Inc. Wallingford CT 2013.
35. S.C.M. ADF2019.302 Theoretical Chemistry, Vrije Universiteit: Amsterdam, 2019. www.scm.com.
36. Schneider, J. A.; Black, H.; Lin, H.-P.; Perepichka, D. F. *ChemPhysChem* **2015**, *16*, 1173–1178.
37. Sun, X.-Q.; Qin, G.-Y.; Lin, P.-P.; Wang, J.; Fan, J.-X.; Li, H.-Y.; Ren, A.-M.; Guo, J.F. *Phys. Chem. Chem. Phys.* **2021**, *23*, 12679–12691.
38. Yin, H.; Geng, Y.; Sun, G.-Y.; Su, Z.-M. *J. Phys. Chem. C* **2017**, *121*, 2125–2134.
39. Belic, J.; van Beek, B.; Menzel, J. P.; Buda, F.; Visscher, L. *J. Phys. Chem. A* **2020**, *124*, 6380–6388.
40. Huang, J.-L.; Rao, B.; Kumar, M. P.; Lu, H.-F.; Chao, I.; Lin, C.-H. *Org. Lett.* **2019**, *21*, 2504–2508.
41. Huang, C.-W.; You, X.; Diemer, P. J.; Petty, A. J.; Anthony, J. E.; Jurchescu, O. D.; Atkin, J. M. *Commun. Chem.* **2019**, *2*, 22.
42. Dong, H.; Wang, C.; Hu, W. *Chem. Commun.* **2010**, *46*, 5211–5222.
43. Usta, H.; Facchetti, A.; Marks, T. J. *Acc. Chem. Res.* **2011**, *44*, 501–510.
44. Murphy, A. R.; Frechet, J. M. J. *Chem. Rev.* **2007**, *107*, 1066–1096.
45. Cagardova, D.; Matuska, J.; Poliak, P.; Lukes, V. *J. Phys. Chem. C* **2019**, *123*, 22752–22766.
46. Quinn, J. T. E.; Zhu, J.; Li, X.; Wang, J.; Li, Y. *J. Mater. Chem. C* **2017**, *5*, 8654–8681.
47. Yu, Y.; Yang, F.; Ji, Y.; Wu, Y.; Zhang, A.; Li, C.; Li, W. *J. Mater. Chem. C* **2016**, *4*, 4134–4137.
48. Gao, J.; Xiao, C.; Jiang, W.; Wang, Z. *Org. Lett.* **2014**, *16*, 394–397.
49. Singh, S. P.; Sellinger, A.; Dodabalapur, A. *J. Appl. Phys.* **2010**, *107*, 044509.
50. Lin, Y.; Li, Y.; Zhan, X. *Chem. Soc. Rev.* **2012**, *41*, 4245–4272.
51. Moral, M.; Garzon-Ruiz, A.; Castro, M.; Canales-Vazquez, J.; Sancho-García, J. C. *J. Phys. Chem. C* **2017**, *121*, 28249–28261.
52. Ahmed, S.; Mushahary, B. C.; Kalita, D. J. *ACS Omega* **2020**, *5*, 8321–8333.
53. Chen, W.-C.; Chao, I. *J. Phys. Chem. C* **2014**, *118*, 20176–20183.
54. Shi, J.-L.; Xiang, S.-Q.; Su, D.-J.; He, R.; Zhao, L.-B. *Phys. Chem. Chem. Phys.* **2021**, *23*, 13159–13169.

55. Amaya, T.; Hirao, T. *Chem. Rec.* **2015**, *15*, 310–321.
56. Wang, J.; Chu, M.; Fan, J. -X.; Lau, T. -K.; Ren, A. -M.; Lu, X.; Miao, Q. *J. Am. Chem. Soc.* **2019**, *141*, 8, 3589–3596.
57. Koh, S. E.; Risko, C.; da Silva Filho, D. A.; Kwon, O.; Facchetti, A.; Brédas, J.-L.; Marks, T. J.; Ratner, M. A. *Adv. Funct. Mater.* **2008**, *18*, 332–340.
58. Lu, X.; Sun, Y.; Hu, W. *J. Mater. Chem. A* **2021**, *9*, 21044-21050.
59. Yin, J.; Chaitanya, K.; Ju, X. -H. *J. Mater. Chem. C* **2015**, *3*, 3472-3481.
60. Lin, L.; Geng, H.; Shuai, Z.; Luo, Y.; *Org. Electron.* **2012**, *13*, 2763-2772.
61. Salerno, F.; Rice, B.; Schmidt, J. A.; Fuchter, M. J.; Nelson, J.; Jelfs, K. E. *Phys. Chem. Chem. Phys.* **2019**, *21*, 5059-5067.
62. Chai, S.; Wen, S. -H.; Huang, J. -D.; Han, K. -L. *J. Comput. Chem.* **2011**, *32*, 3218-3225.
63. Park, K. S.; Kwok, J. J.; Dilmurat, R.; Qu, G.; Kafle, P.; Luo, X.; Jung, S. -H.; Olivier, Y.; Lee, J. -K.; Mei, J.; Beljonne, D.; Diao, Y. *Sci. Adv.* **2019**, *5*, eaaw7757.

Supporting Information

Table S1. Comparison of the frontier molecular orbital (FMO) energies of DCP-1, 2, and 3, calculated at different density functional theory (DFT) methods using 6-311G(d,p) basis set, with the experimental values. (B3LYP: 20% HF, PBE0: 25% HF).

Compound	Method	HOMO (eV)	LUMO (eV)	E _g (eV)
DCPP-1	Expt.	-5.48	-3.08	2.40
	B3LYP	-5.666	-2.664	3.002
	PBE0	-5.851	-2.552	3.299
	B3LYP-D3	-5.665	-2.663	3.002
	B3LYP-D3(BJ)	-5.667	-2.665	3.002
DCPP-2	Expt.	-5.50	-3.29	2.21
	B3LYP	-5.662	-2.967	2.695
	PBE0	-5.841	-2.869	2.972
	B3LYP-D3	-5.668	-2.951	2.717
	B3LYP-D3(BJ)	-5.671	-2.949	2.722
DCPP-3	Expt.	-5.46	-2.70	2.76
	B3LYP	-5.673	-3.216	2.457
	PBE0	-5.854	-3.134	2.720
	B3LYP-D3	-5.685	-3.201	2.484
	B3LYP-D3(BJ)	-5.687	-3.198	2.489

Table S2: Front and side views of B3LYP/6-311G(d,p) optimized molecular geometries of the experimentally available [S1] DCP-TPMP-1, 2, 3 molecules (TPMP: p-trifluoromethylphenyl groups).


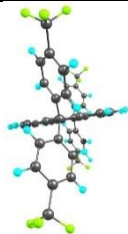
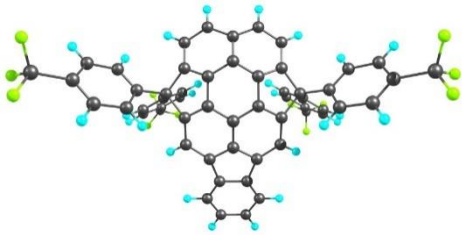
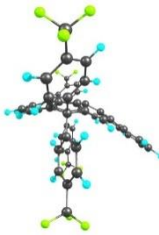
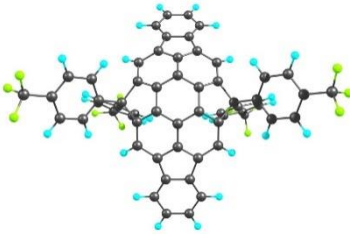

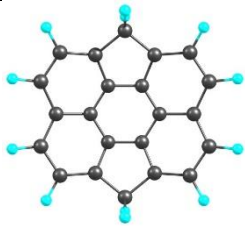
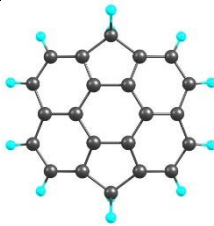

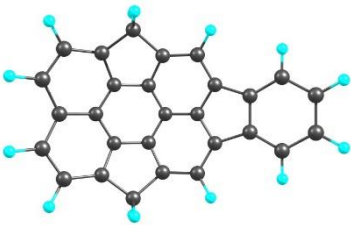
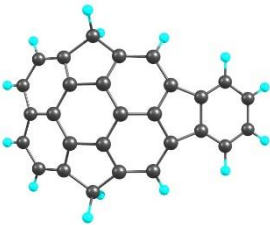
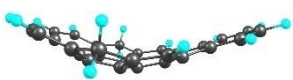
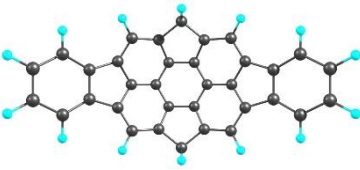


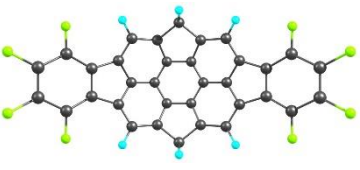



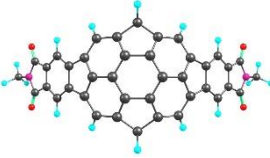

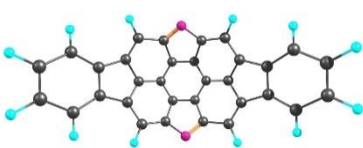





Compound	Front view	Side view
DCPP-TPMP-1		
DCPP-TPMP-2		
DCPP-TPMP-3		

Table S3. Front and side views of B3LYP/6-311G(d,p) optimized molecular geometries of DCPD compounds.

Compound d	Front view		Side view
	Concave surface	Convex surface	
DCPD-1			
DCPD-2			
DCPD-3			
DCPD-4			
DCPD-5			
DCPD-6			
DCPD-7			

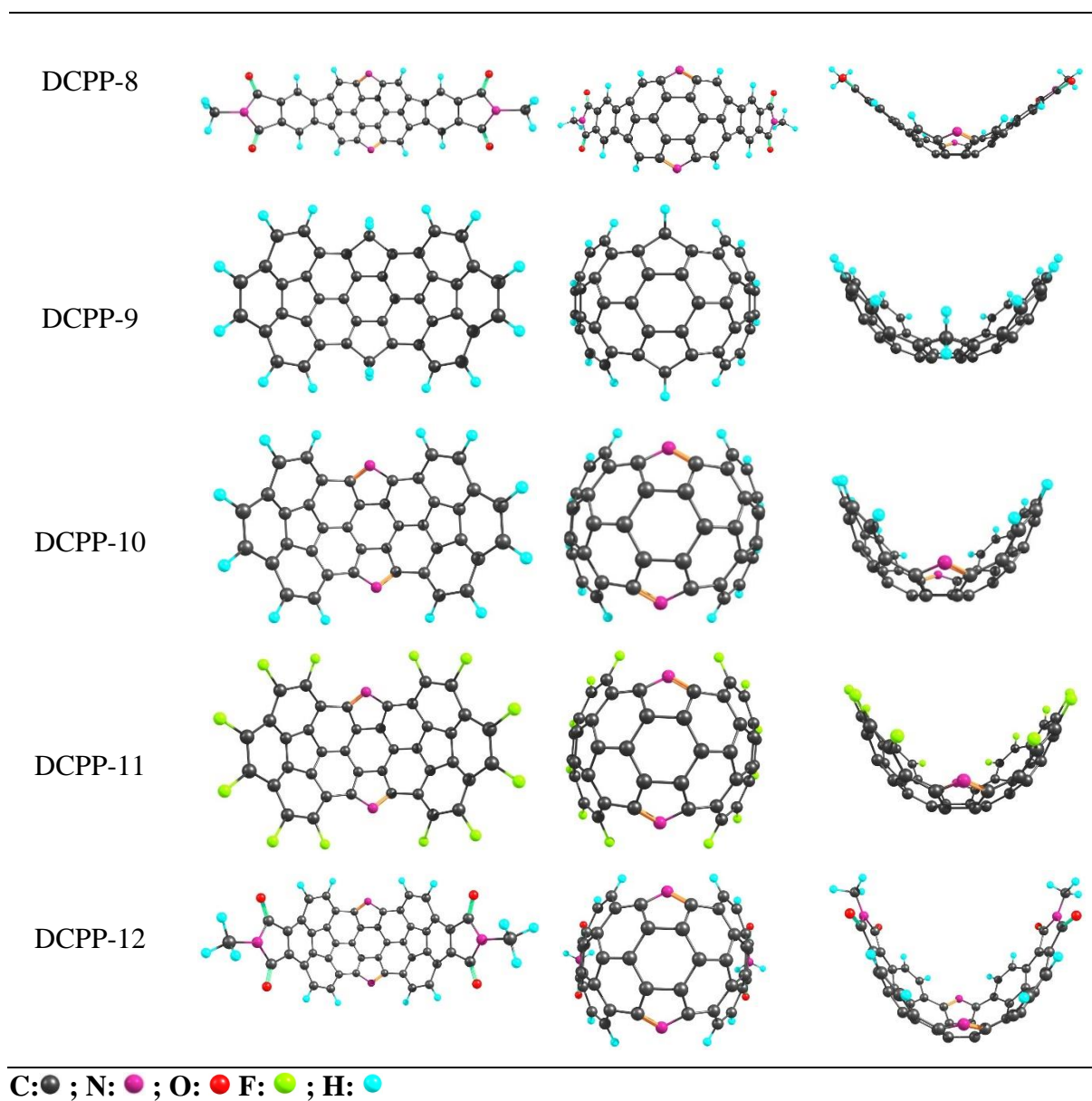
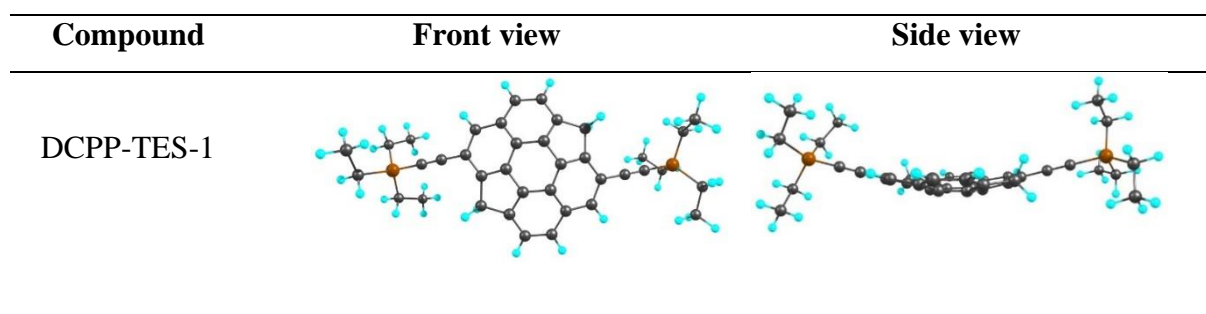
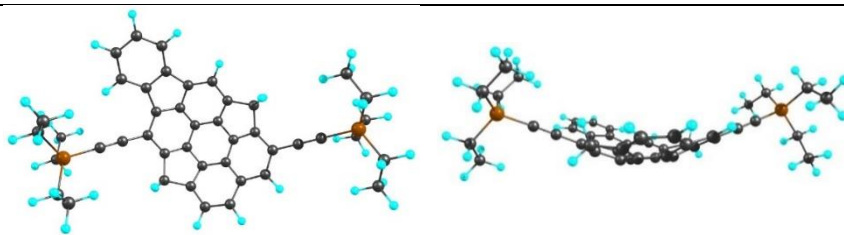


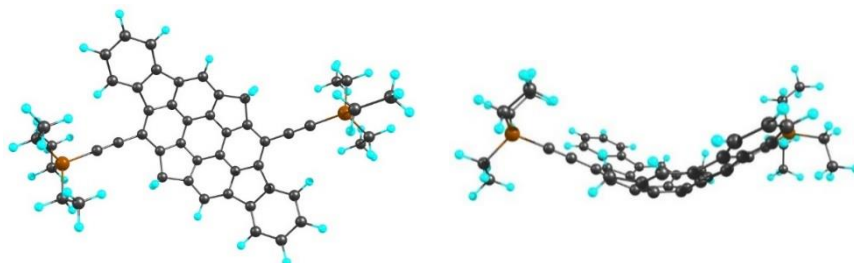
Table S4. Front and side views of B3LYP/6-311G(d,p) optimized molecular geometries of DCPP compounds with TES side chains.



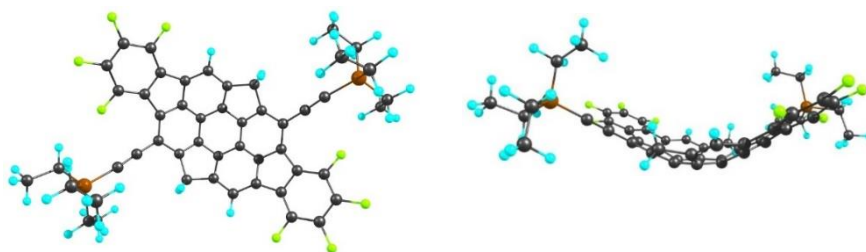
DCPP-TES-2



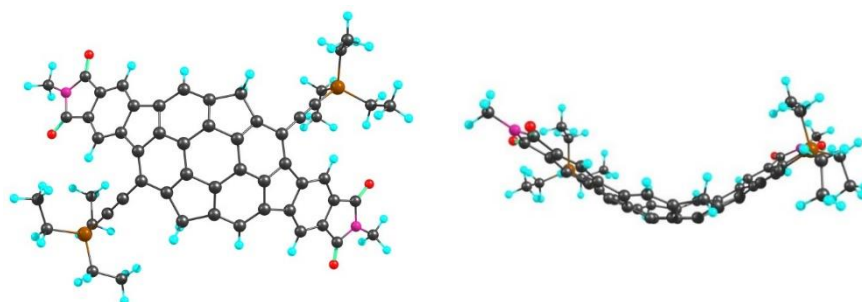
DCPP-TES-3



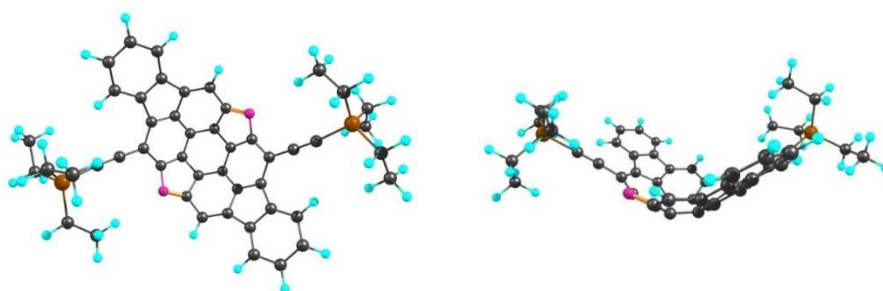
DCPP-TES-4



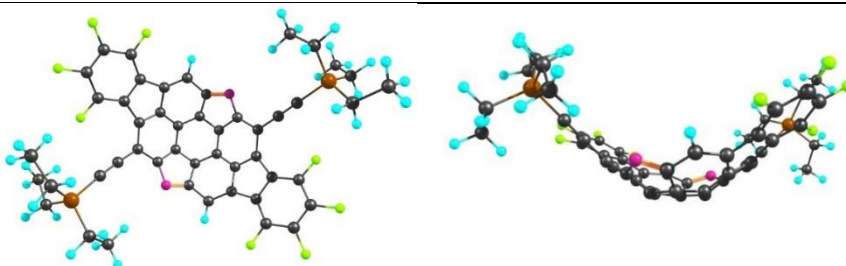
DCPP-TES-5



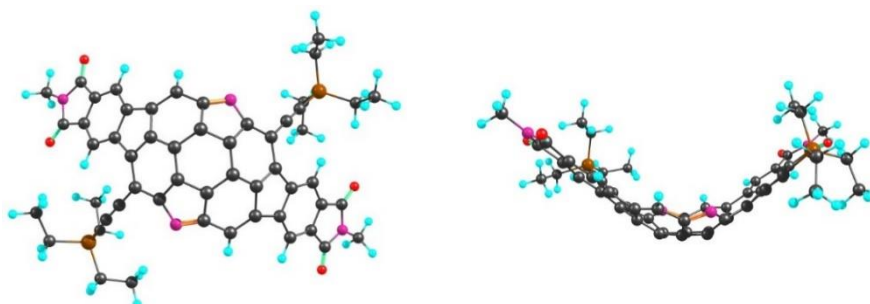
DCPP-TES-6



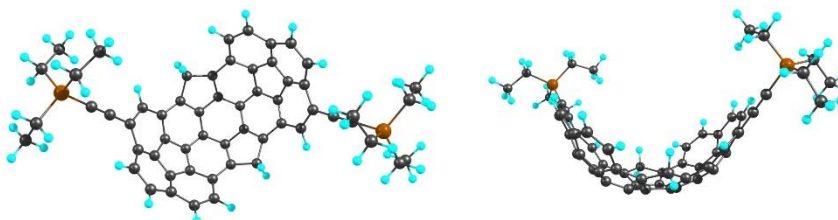
DCPP-TES-7



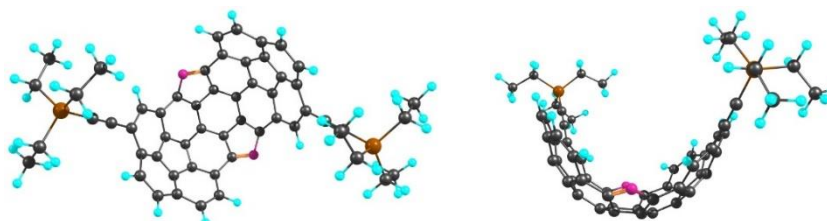
DCPP-TES-8



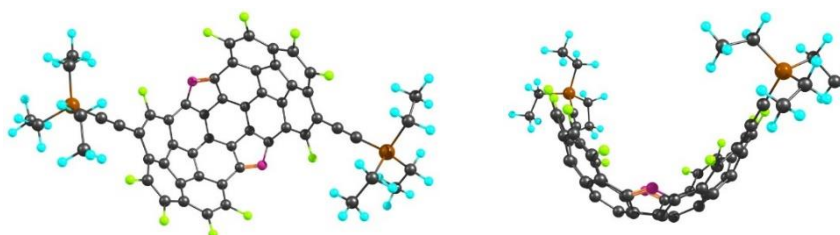
DCPP-TES-9



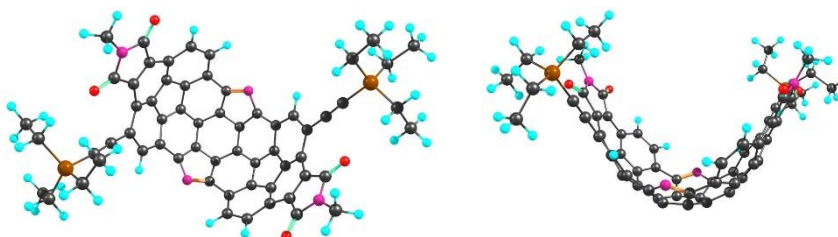
DCPP-TES-10



DCPP-TES-11



DCPP-TES-12

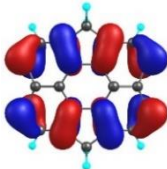
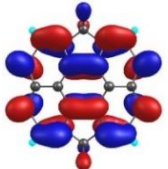
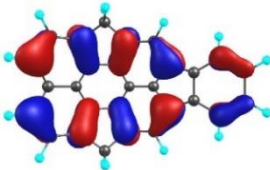
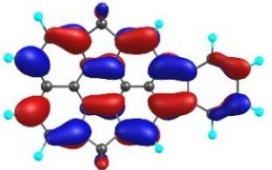
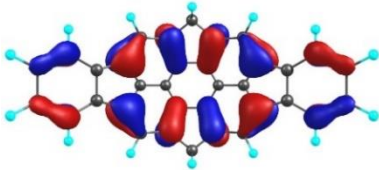
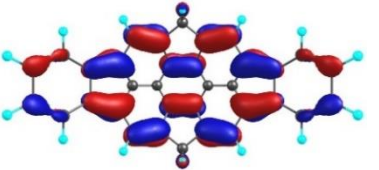
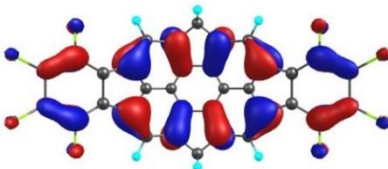
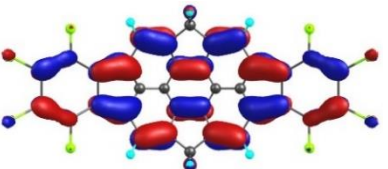
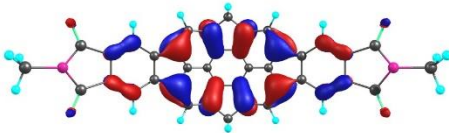
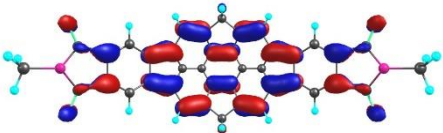
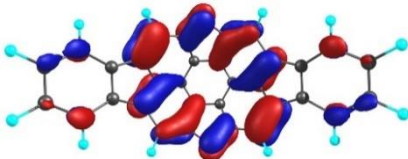
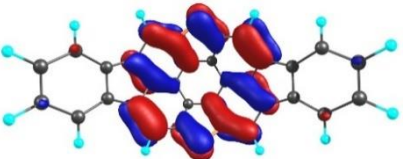
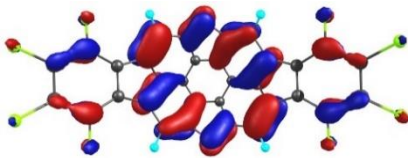
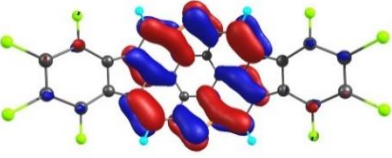


C: ; N: ; O: ; F: ; Si: ; H:

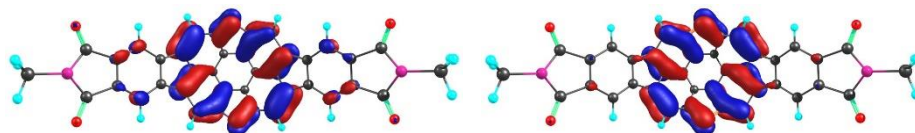
Table S5. Bowl depths, cone angles, dipole moments (μ), bowl-to-bowl inversion barriers, HOMOs, LUMOs and HOMO-LUMO gaps (E_g) of the DCPD and DCPD-TES derivatives.

Compound	Bowl depth (Å)	Cone angle (°)	BWBI	HOMO (eV)	LUMO (eV)	E _g (eV)
DCPD-1	0.595	147.06		-5.048	-1.919	3.129
DCPD-2	----	----		-5.133	-2.349	2.784
DCPD-3	3.007	119.64		-5.205	-2.661	2.544
DCPD-4	3.035	118.89		-5.739	-3.267	2.472
DCPD-5	4.144	118.53		-5.8	-3.408	2.392
DCPD-6	3.640	106.13		-5.778	-4.113	1.665
DCPD-7	3.677	105.13		-6.285	-4.644	1.641
DCPD-8	4.967	105.05		-6.309	-4.646	1.663
DCPD-9	4.104	86.77		-5.421	-2.47	2.951
DCPD-10	4.542	75.70		-5.705	-4.264	1.441
DCPD-11	4.479	77.73		-6.57	-5.157	1.413
DCPD-12	6.584	65.21		-6.139	-4.704	1.435
DCPD-TES-1	0.590	146.85		-5.225	-2.174	3.051
DCPD-TES-2	----	----		-5.258	-2.54	2.718
DCPD-TES-3	2.938	121.20		-5.285	-2.782	2.503
DCPD-TES-4	3.035	123.46		-5.746	-3.317	2.429
DCPD-TES-5	4.164	118.21		-5.8	-3.443	2.357
DCPD-TES-6	3.520	108.90		-5.692	-4.173	1.519
DCPD-TES-7	3.398	111.43		-6.102	-4.598	1.504
DCPD-TES-8	4.843	107.23		-6.124	-4.597	1.527
DCPD-TES-9	4.109	53.67		-5.505	-2.578	2.927
DCPD-TES-10	4.539	75.86		-5.692	-4.3	1.392
DCPD-TES-11	4.471	77.89		-6.315	-4.962	1.353
DCPD-TES-12	6.466	69.72		-6.025	-4.679	1.346

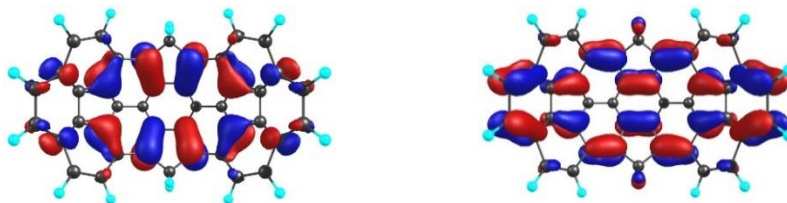
Table S6. Distribution of frontier molecular orbitals (HOMO and LUMO) of the DCPD compounds computed at B3LYP/6-311G(d,p) level.

Compound	HOMO	LUMO
DCPD-1		
DCPD-2		
DCPD-3		
DCPD-4		
DCPD-5		
DCPD-6		
DCPD-7		

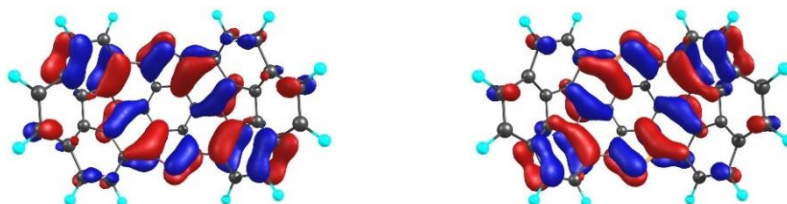
DCPP-8



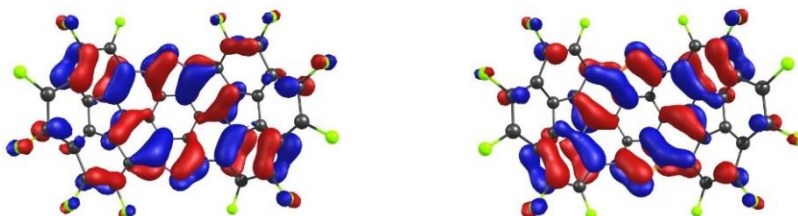
DCPP-9



DCPP-10



DCPP-11



DCPP-12

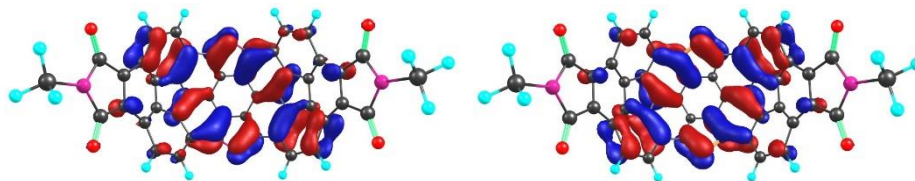
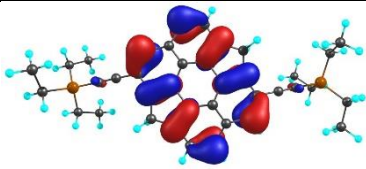
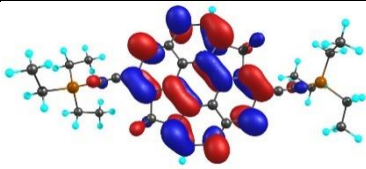
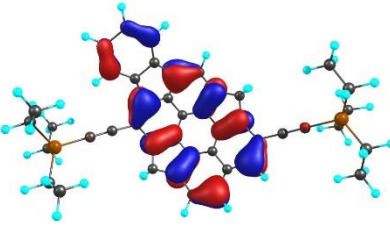
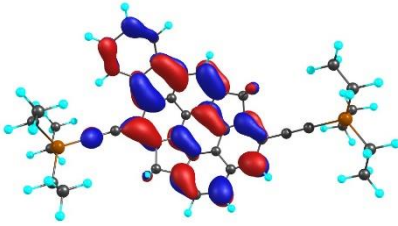
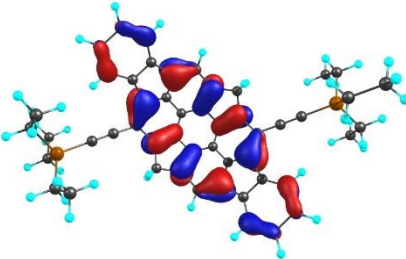
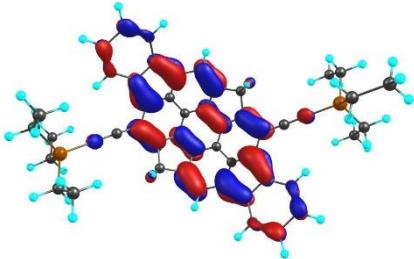
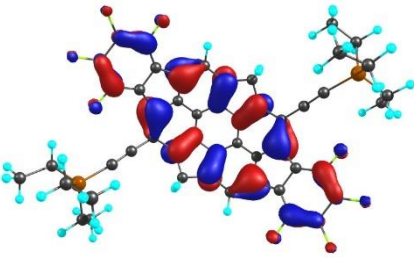
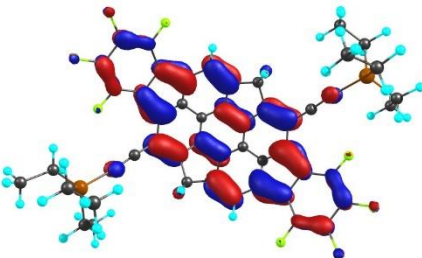
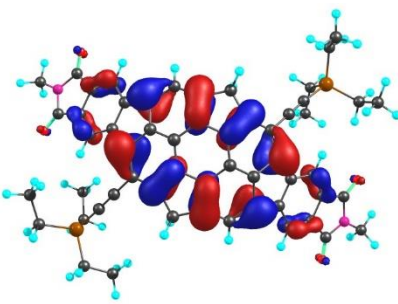
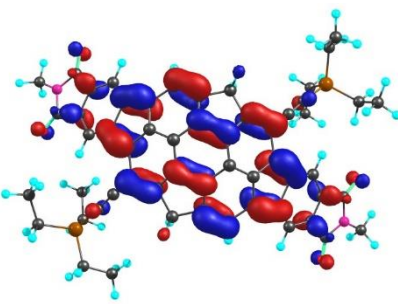
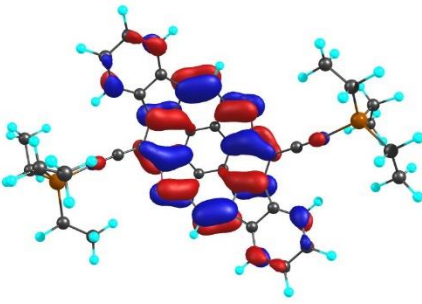
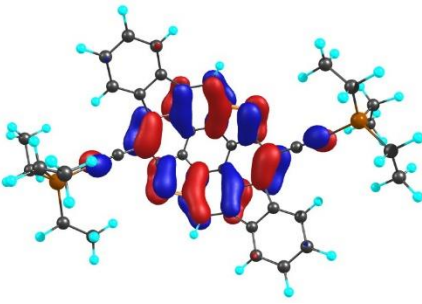
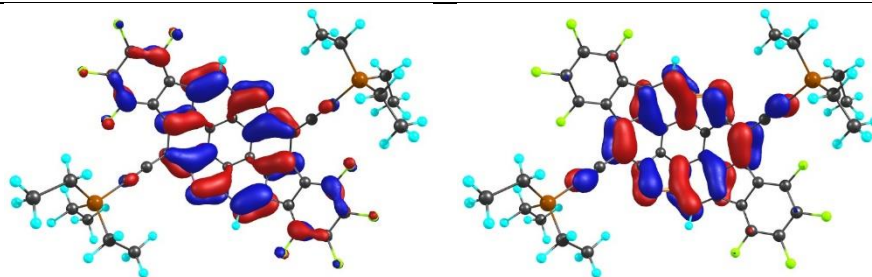


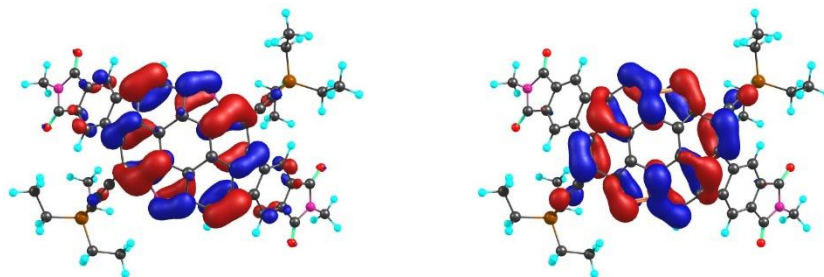
Table S7. Distribution of frontier molecular orbitals (HOMO and LUMO) of the DCP-PP-TES compounds computed at B3LYP/6-311G(d,p) level.

Compound	HOMO	LUMO
DCPP-TES-1		
DCPP-TES-2		
DCPP-TES-3		
DCPP-TES-4		
DCPP-TES-5		
DCPP-TES-6		

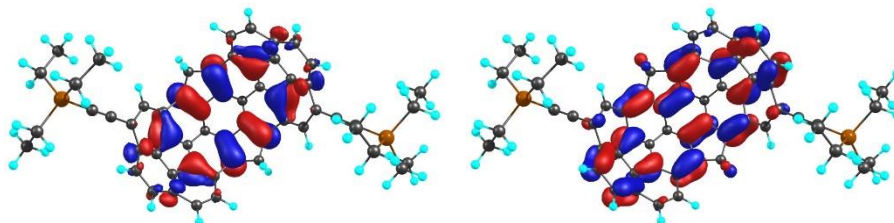
DCPP-TES-7



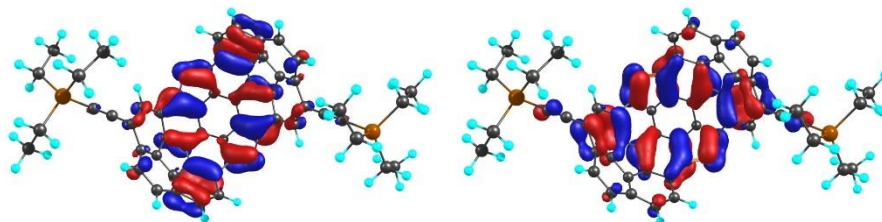
DCPP-TES-8



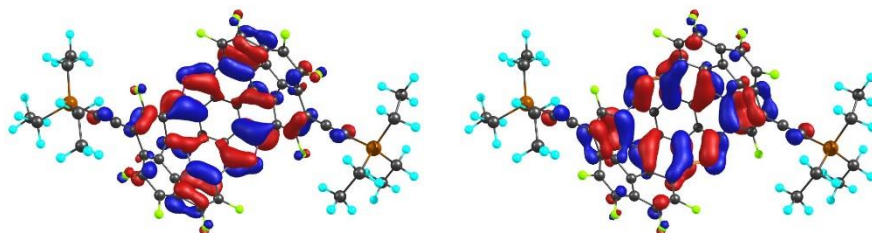
DCPP-TES-9



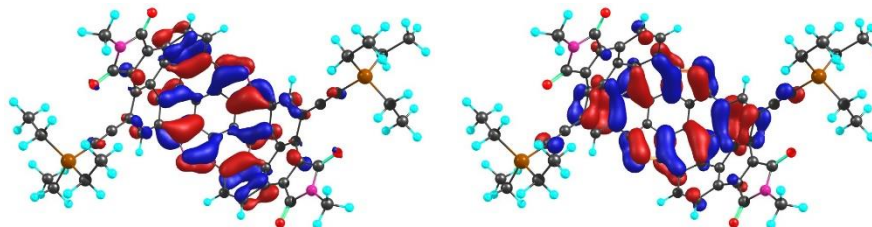
DCPP-TES-10



DCPP-TES-11



DCPP-TES-12



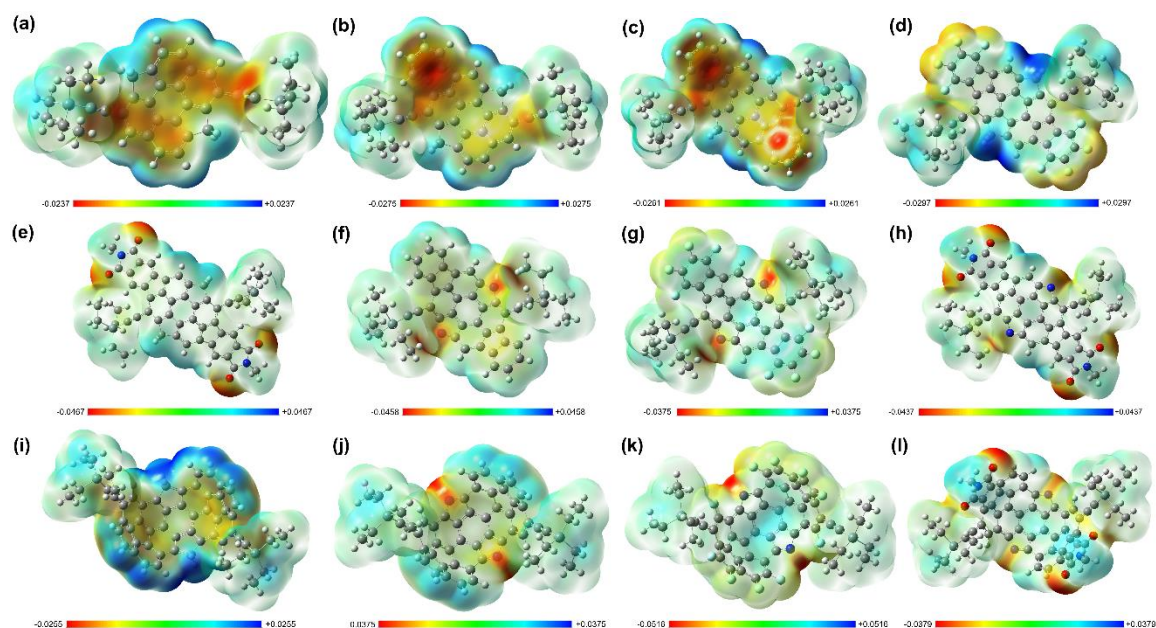


Figure S1. Electrostatic potential (ESP) mapping of DCPD-TES compounds.

Section S1. Predicting the crystal structures of DCPD-derivatives.

Crystal structure predictions are conducted over the Polymorph Predictor module in BIOVIA Materials Studio program (17.1.0.48) [S2], using the previously optimized molecular geometries. All the crystal structures of DCPD-derivatives are obtained with the fine quality simulation, using Dreiding forcefield, as discussed in our previous work [S3]. However, we chose Gasteiger and ESP charges separately for generating the molecular packing motifs of DCPDs and DCPD-TESs, respectively. Each molecule is allowed to pack into the following space groups; $P2_1/c$, $P1$, $P2_12_12_1$, $C2/c$, $P2_1$, $Pbca$, $Pna2_1$, $Pbcn$, Cc , and $C2$, out of which the crystal with lowest lattice energy is selected for the further studies [S4, S5].

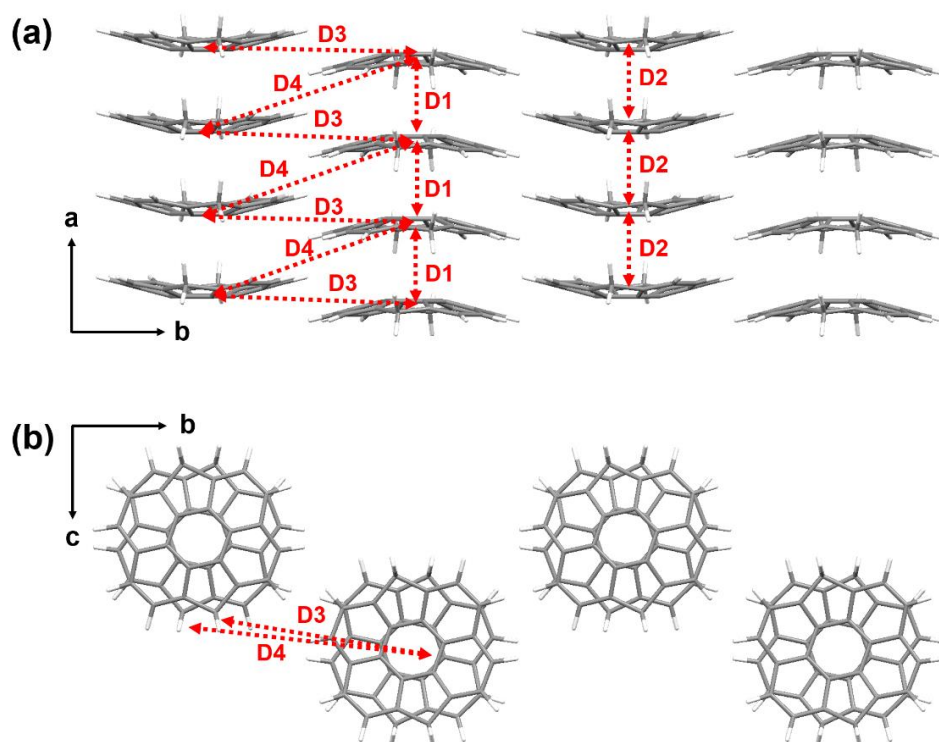


Figure S2. Crystal structure of DCP1 showing different conducting channels: (a) side view and (b) top view.

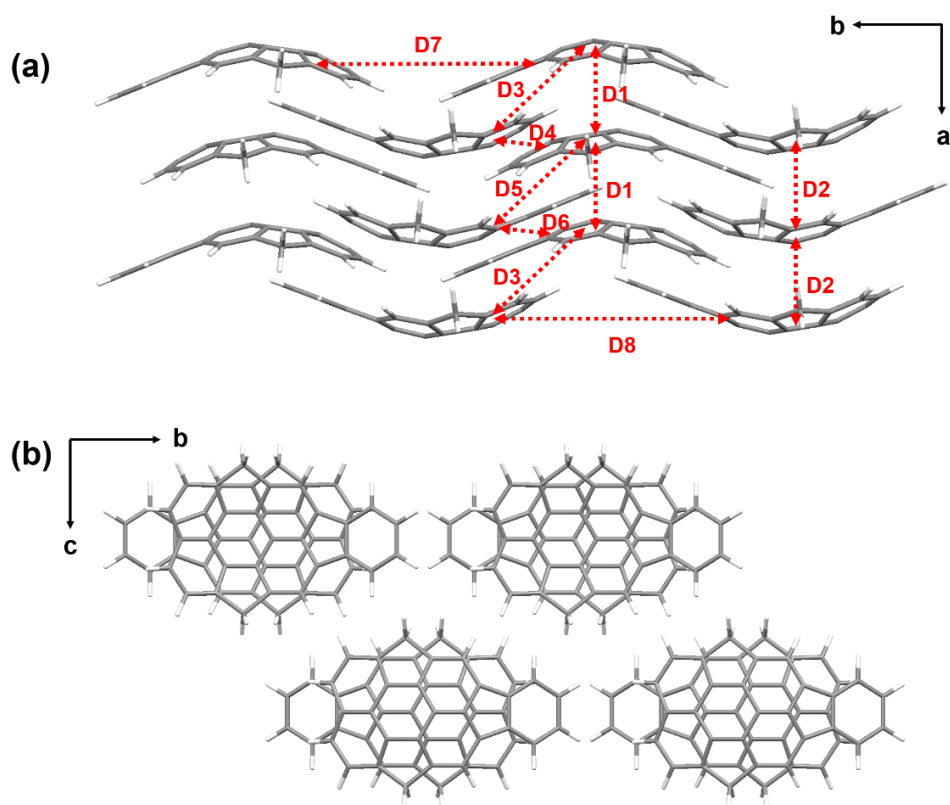


Figure S3. Crystal structure of DCP2 showing different conducting channels: (a) side view and (b) top view.

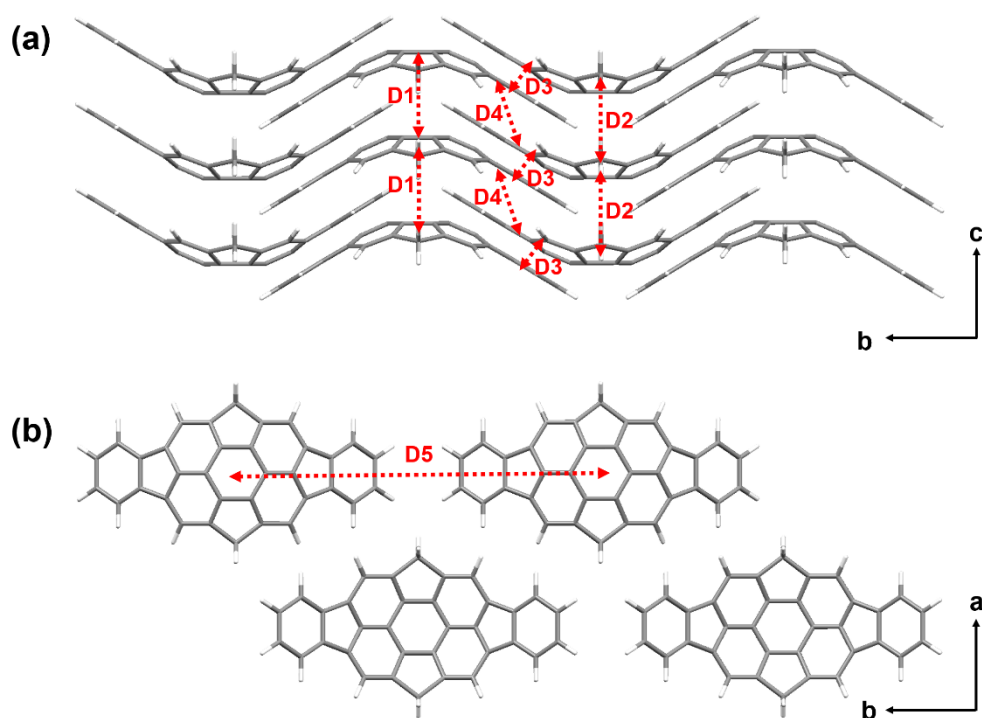


Figure S4. Crystal structure of DCP3 showing different conducting channels: (a) side view and (b) top view.

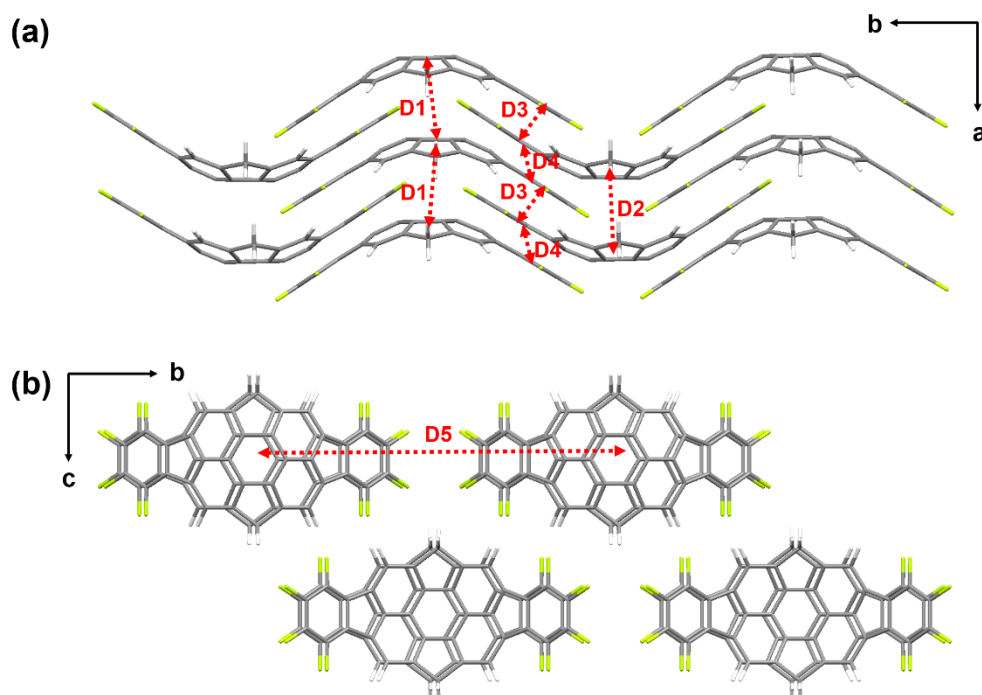


Figure S5. Crystal structure of DCP4 showing different conducting channels: (a) side view and (b) top view.

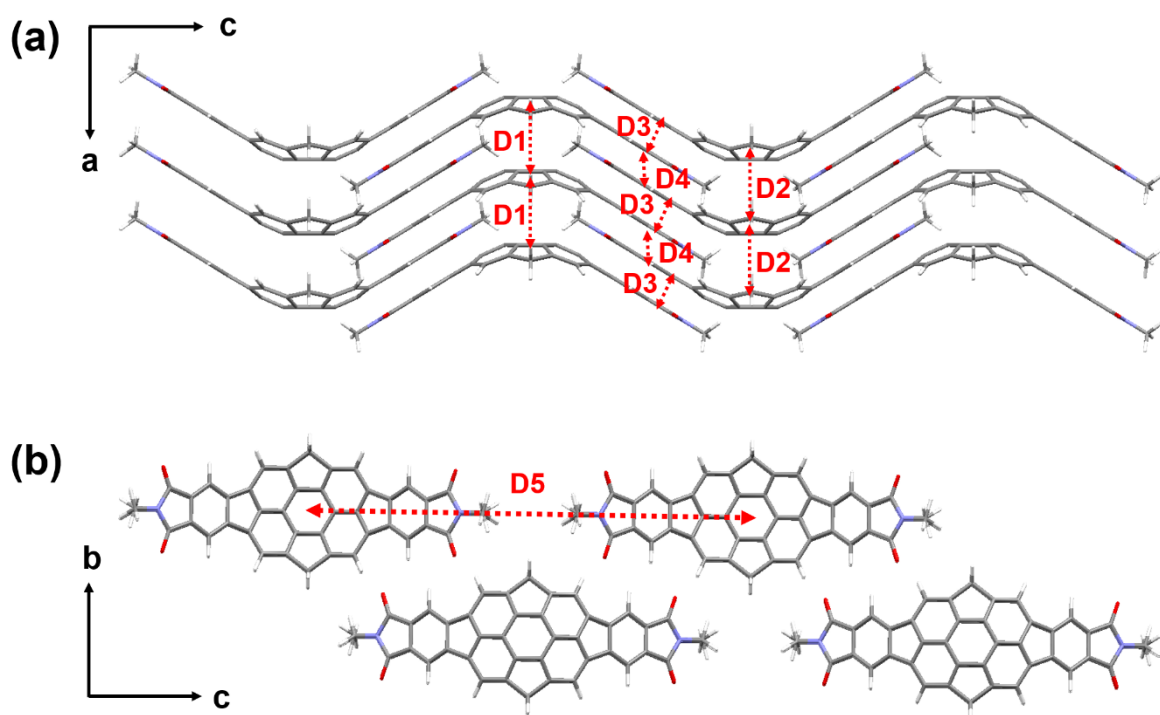


Figure S6. Crystal structure of DCP5 showing different conducting channels: (a) side view and (b) top view.

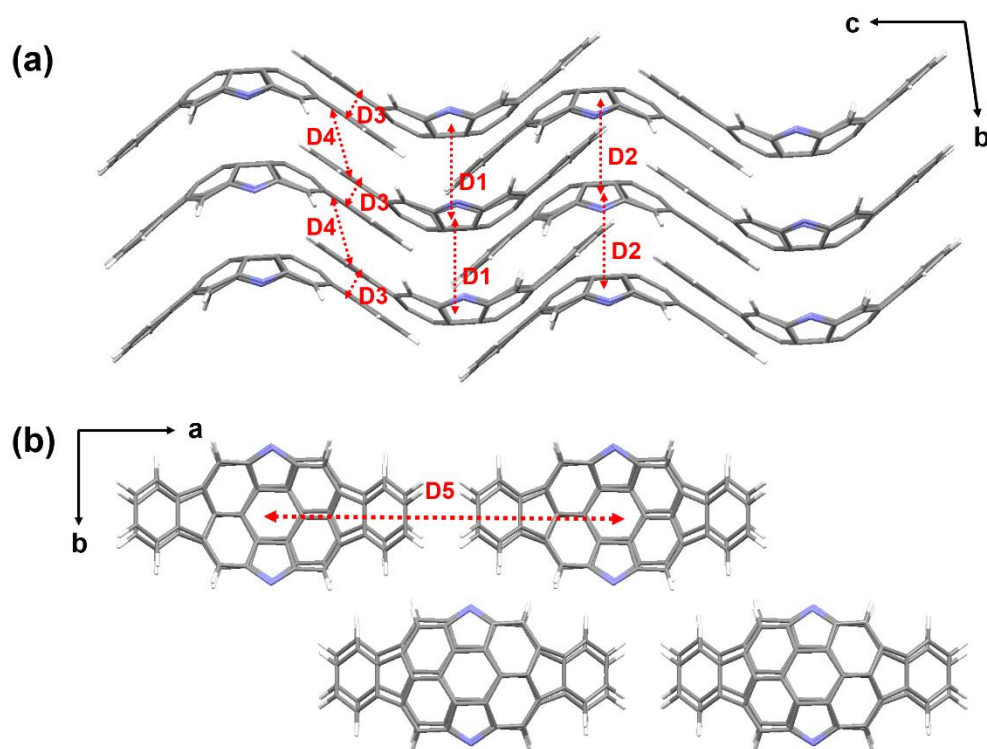


Figure S7. Crystal structure of DCP6 showing different conducting channels: (a) side view and (b) top view.

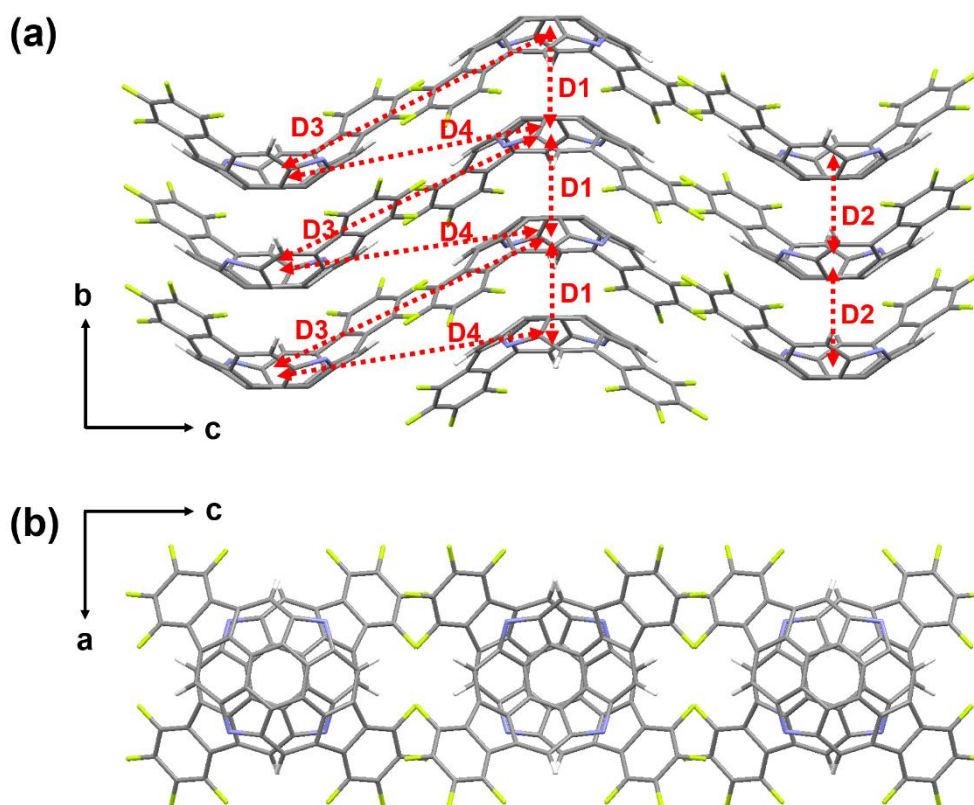


Figure S8. Crystal structure of DCP7 showing different conducting channels: (a) side view and (b) top view.

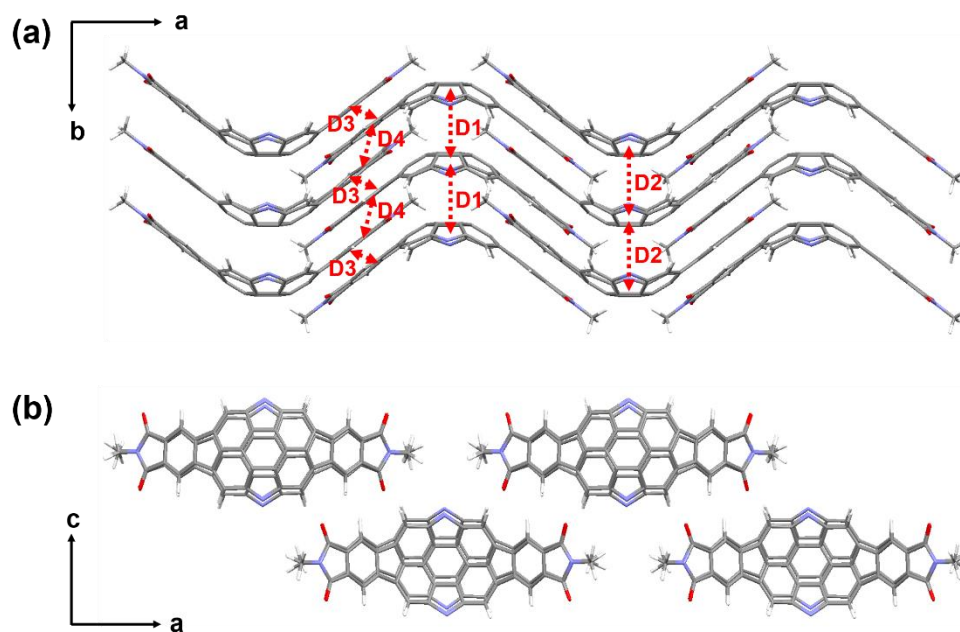


Figure S9. Crystal structure of DCP8 showing different conducting channels: (a) side view and (b) top view.

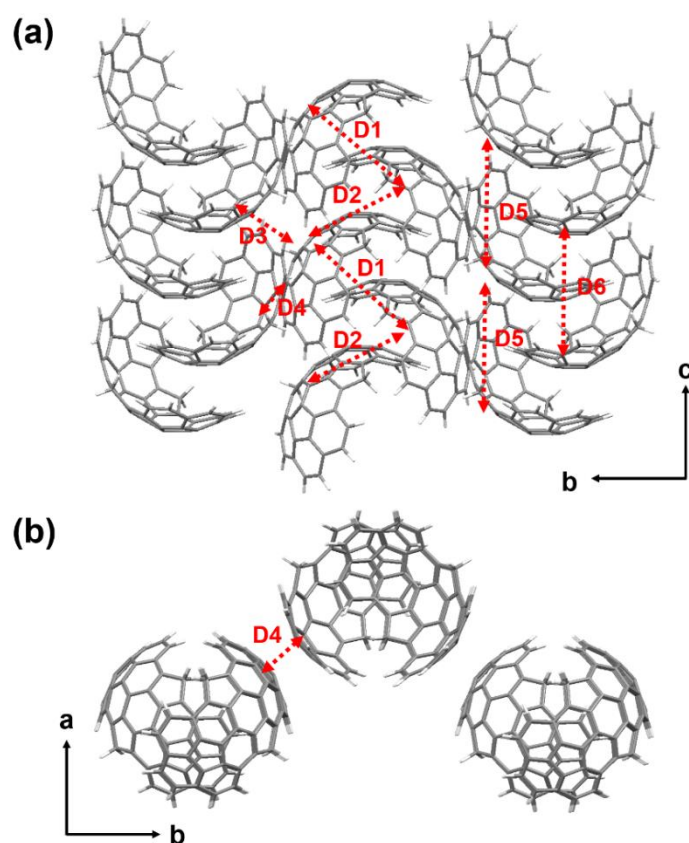


Figure S10. Crystal structure of DCP9 showing different conducting channels: (a) side view and (b) top view.

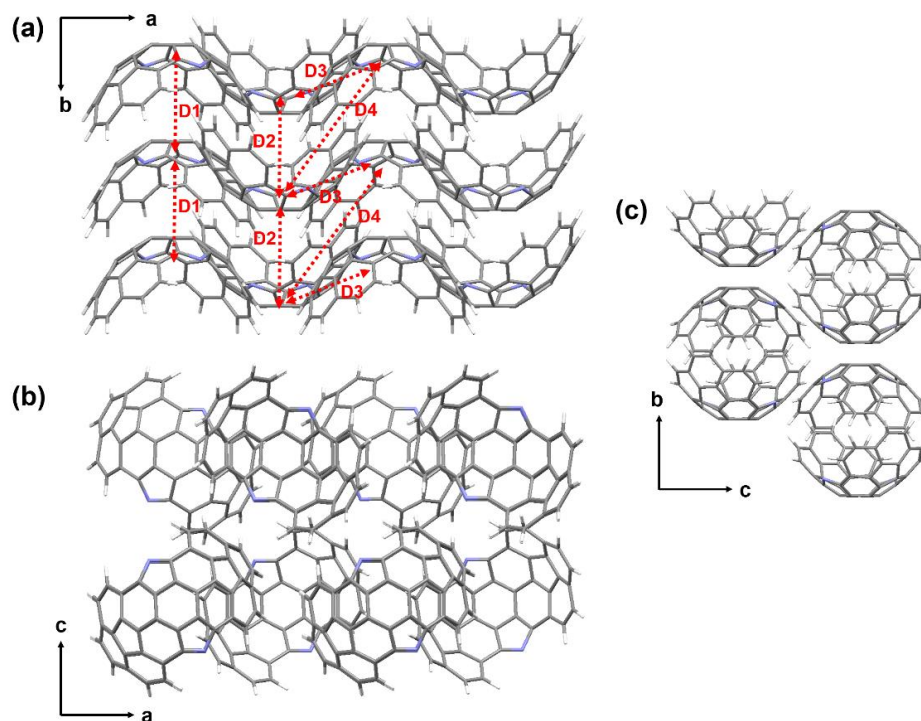


Figure S11. Crystal structure of DCP10 showing different conducting channels: (a) side view and (b) top view.

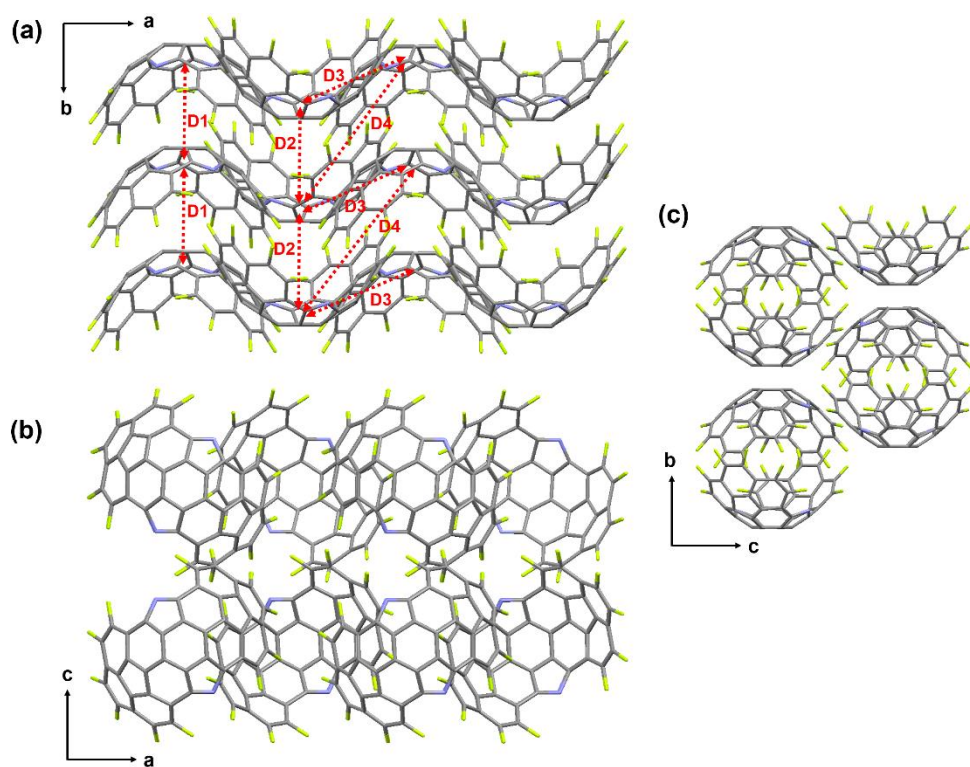


Figure S12. Crystal structure of DCP11 showing different conducting channels: (a) side view and (b) top view.

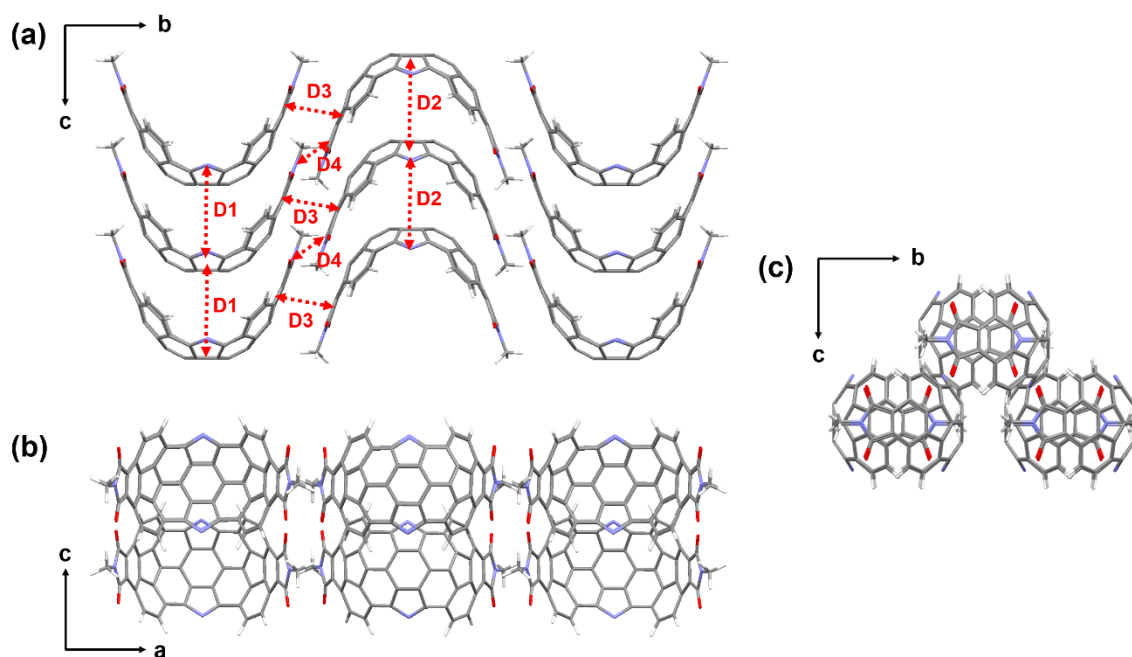


Figure S13. Crystal structure of DCP12 showing different conducting channels: (a) side view and (b) top view.

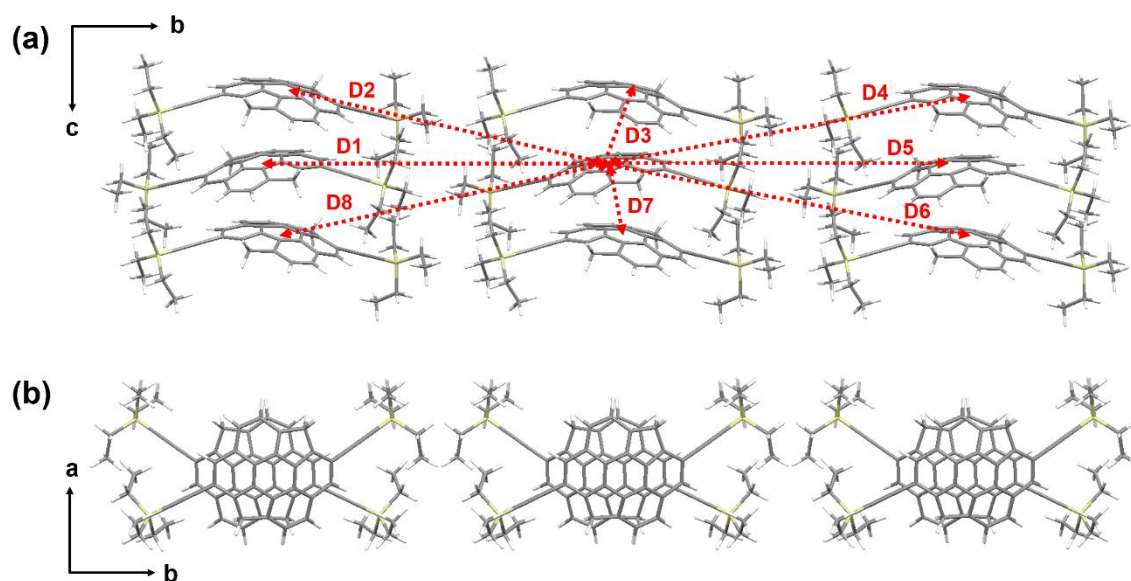


Figure S14. Crystal structure of DCPPI-TES showing different conducting channels: (a) side view and (b) top view.

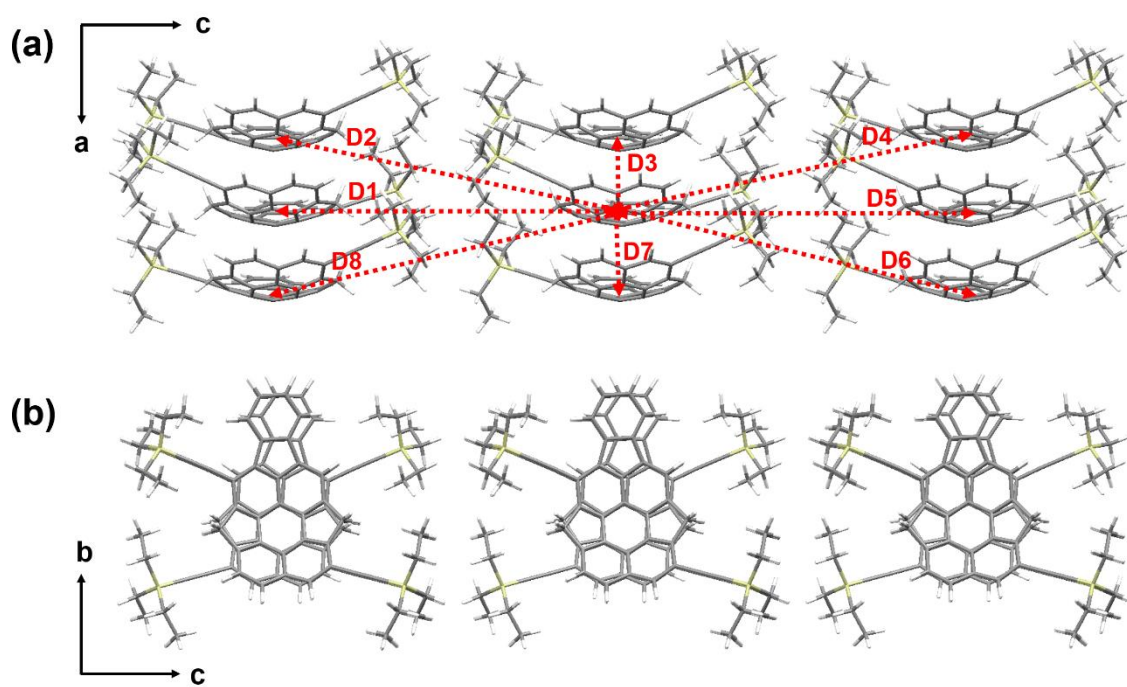


Figure S15. Crystal structure of DCPPI2-TES showing different conducting channels: (a) side view and (b) top view.

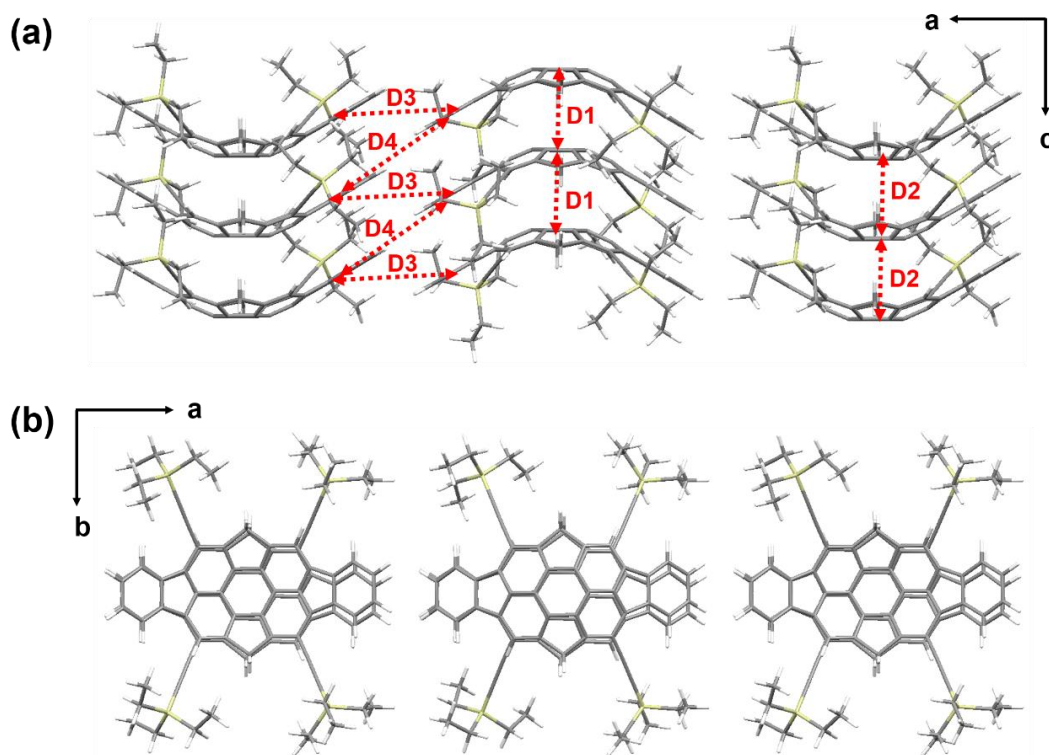


Figure S16. Crystal structure of DCP3-TES showing different conducting channels: (a) side view and (b) top view.

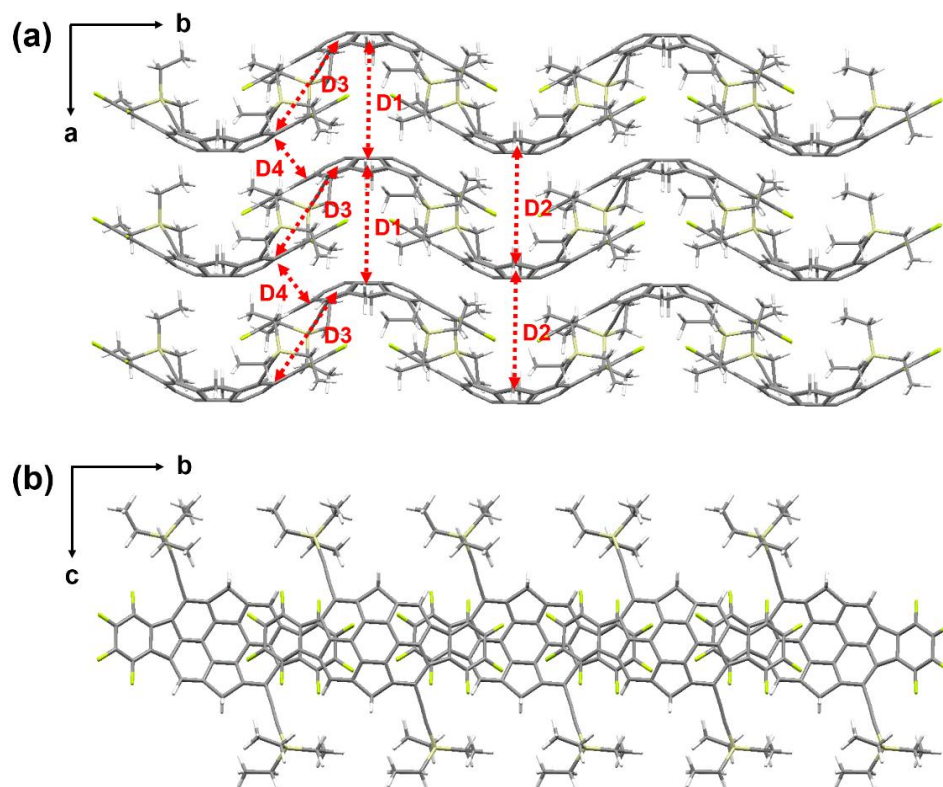


Figure S17. Crystal structure of DCP4-TES showing different conducting channels: (a) side view and (b) top view.

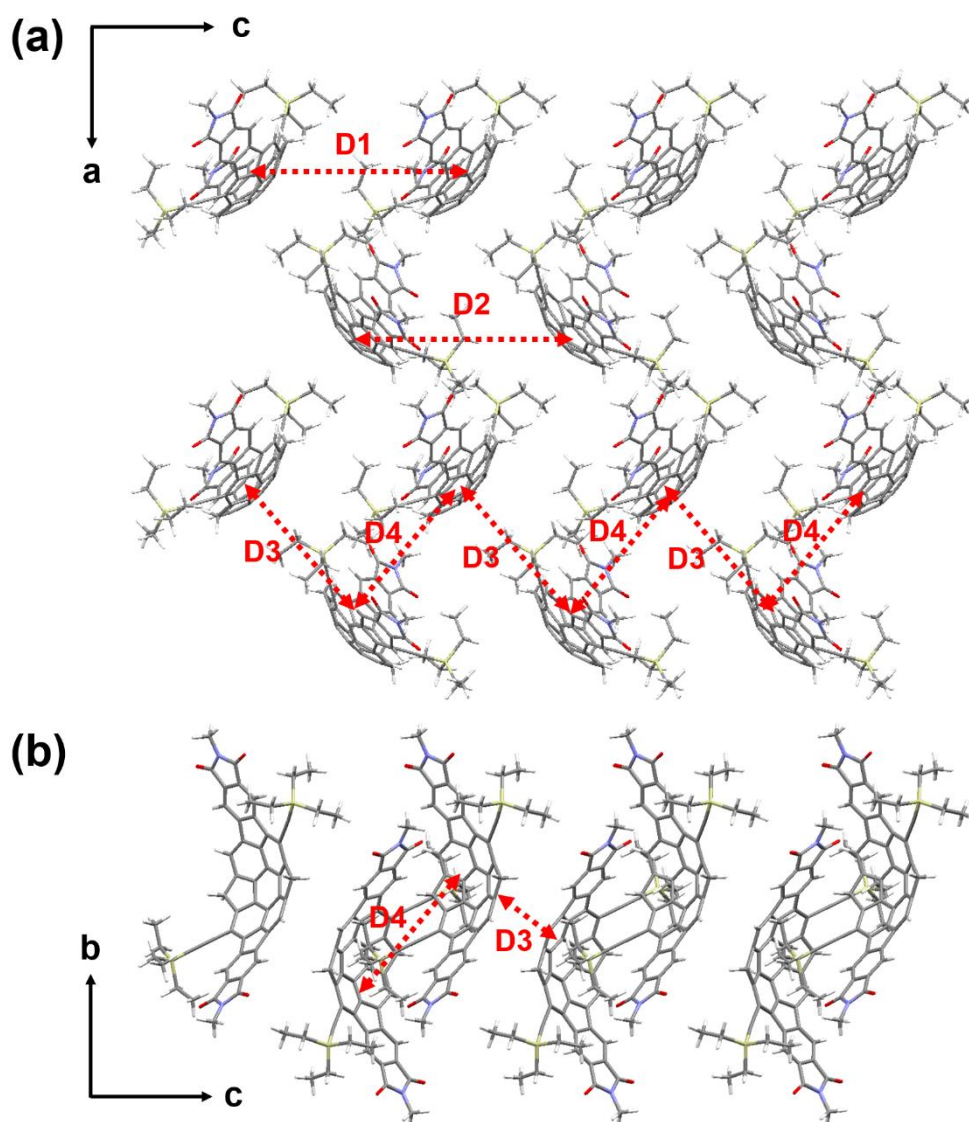


Figure S18. Crystal structure of DCP5-TES showing different conducting channels: (a) side view and (b) top view.

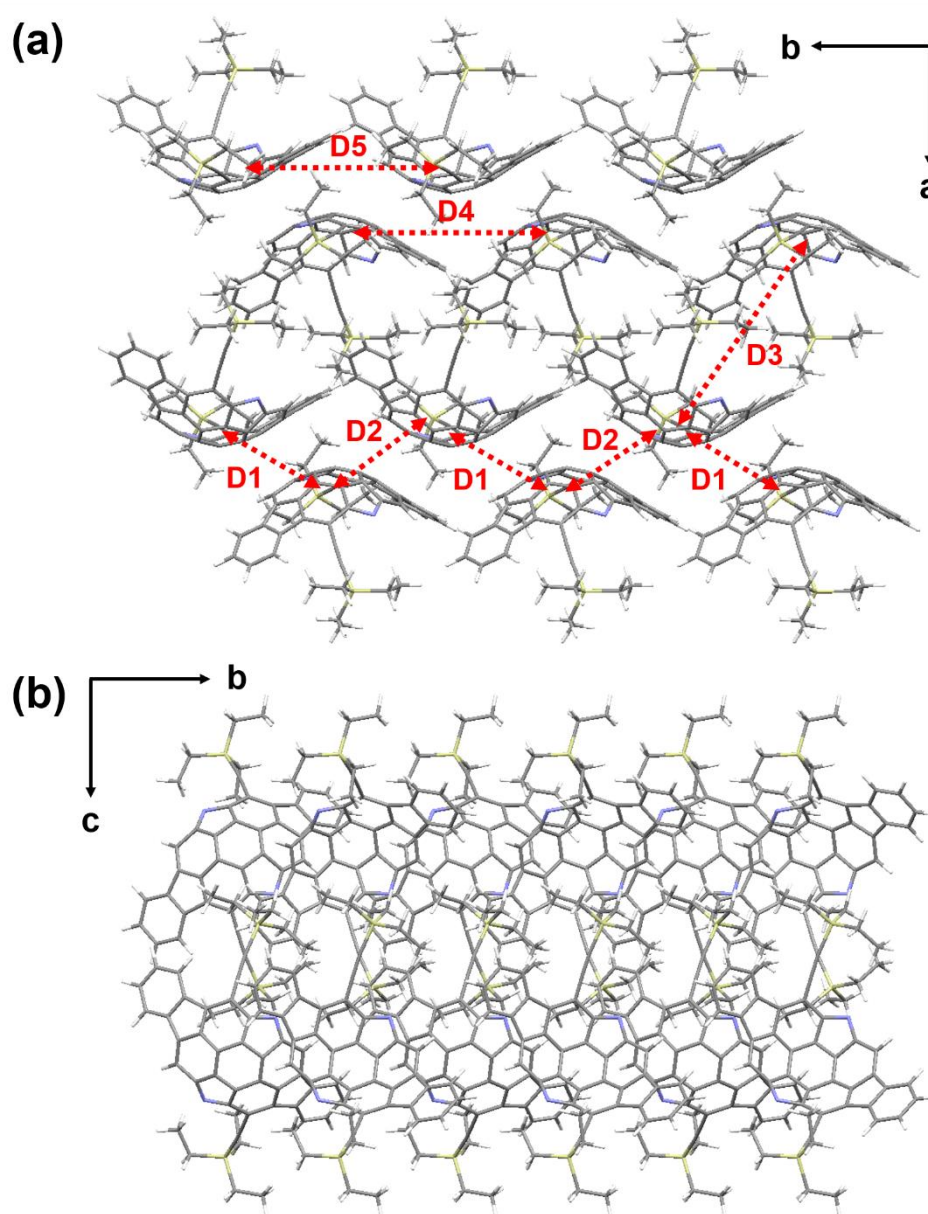


Figure S19. Crystal structure of DCP6-TES showing different conducting channels: (a) side view and (b) top view.

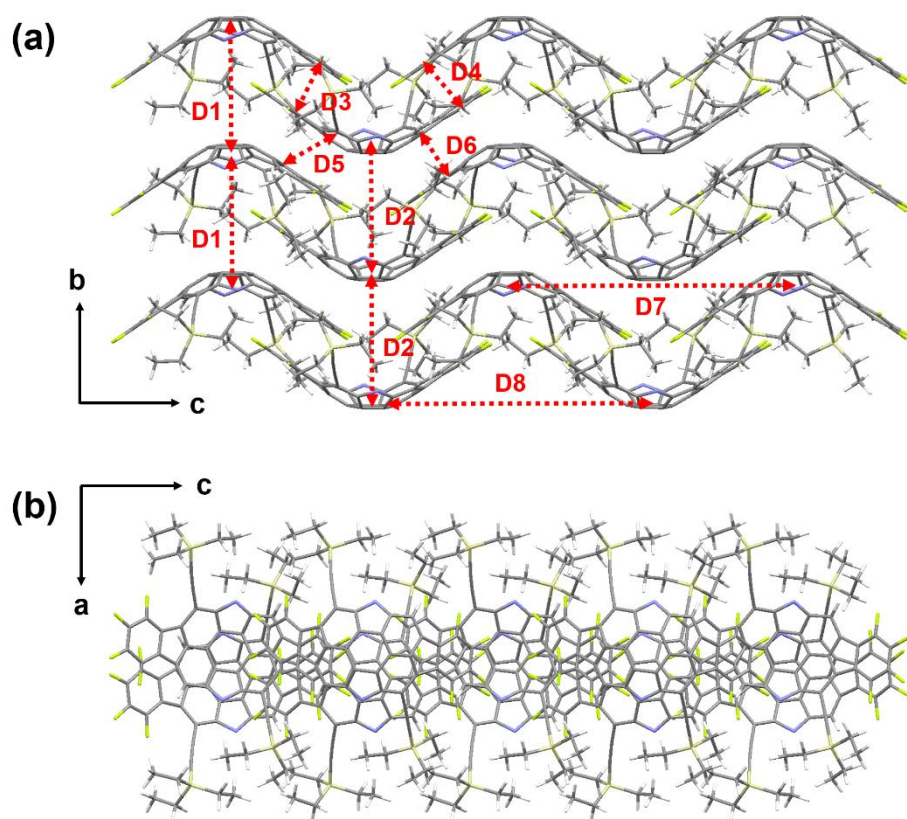


Figure S20. Crystal structure of DCP7-TES showing different conducting channels: (a) side view and (b) top view.

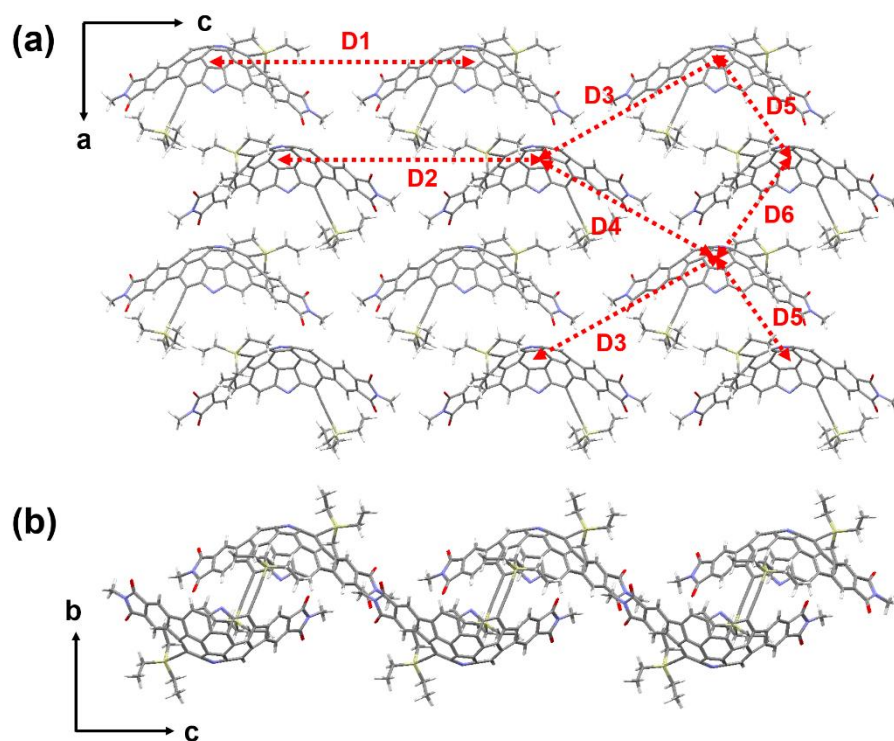


Figure S21. Crystal structure of DCP8-TES showing different conducting channels: (a) side view and (b) top view.

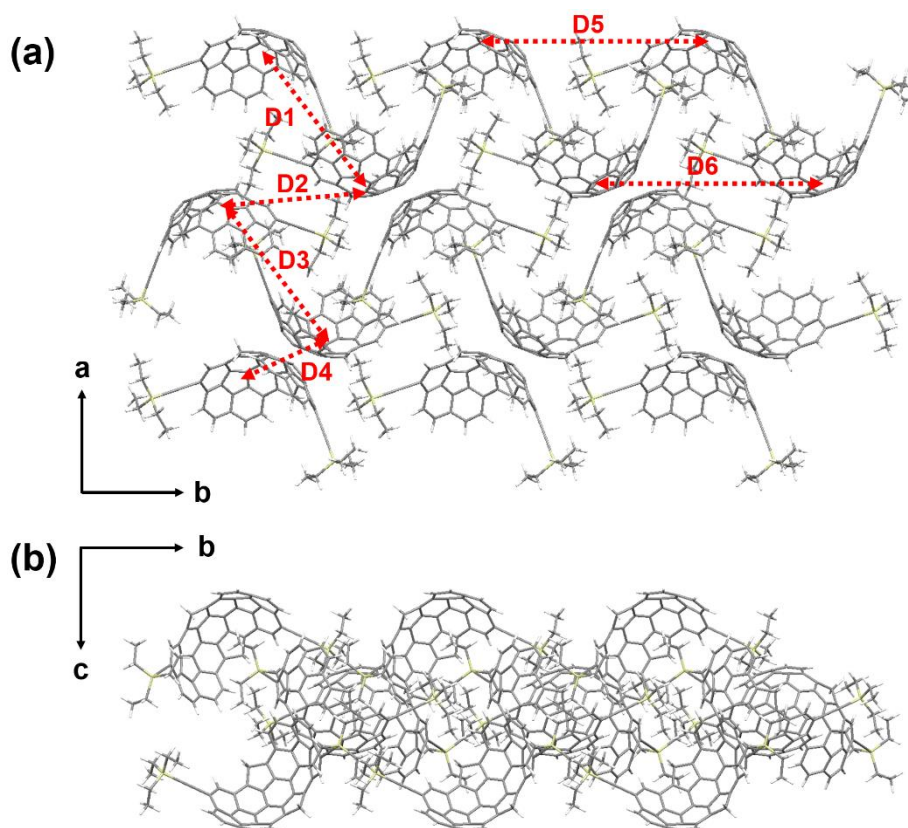


Figure S22. Crystal structure of DCP9-TES showing different conducting channels: (a) side view and (b) top view.

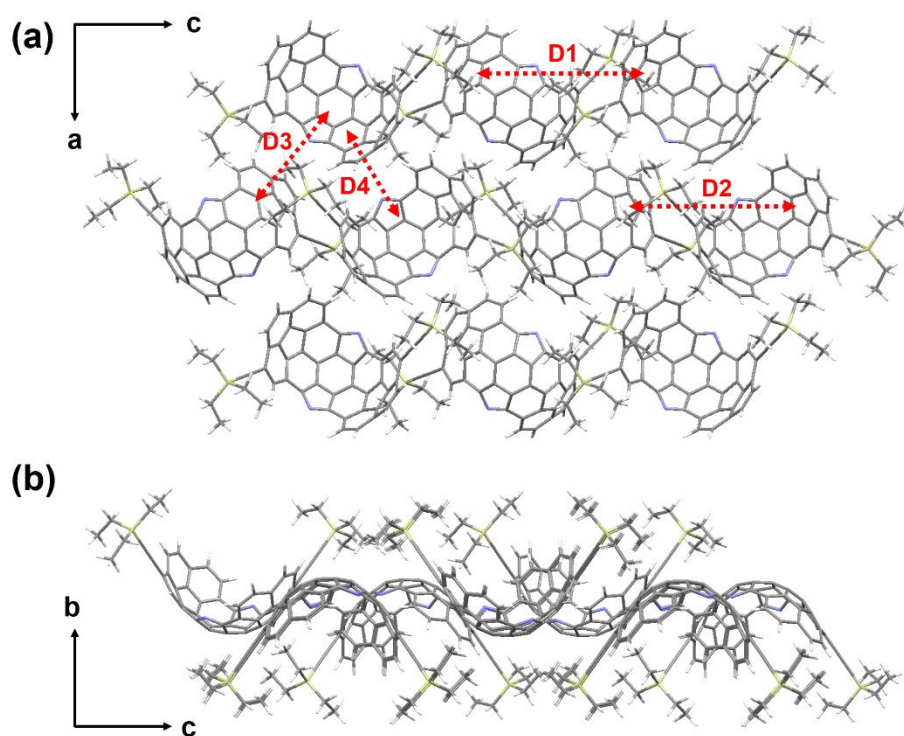


Figure S23. Crystal structure of DCP10-TES showing different conducting channels: (a) side view and (b) top view.

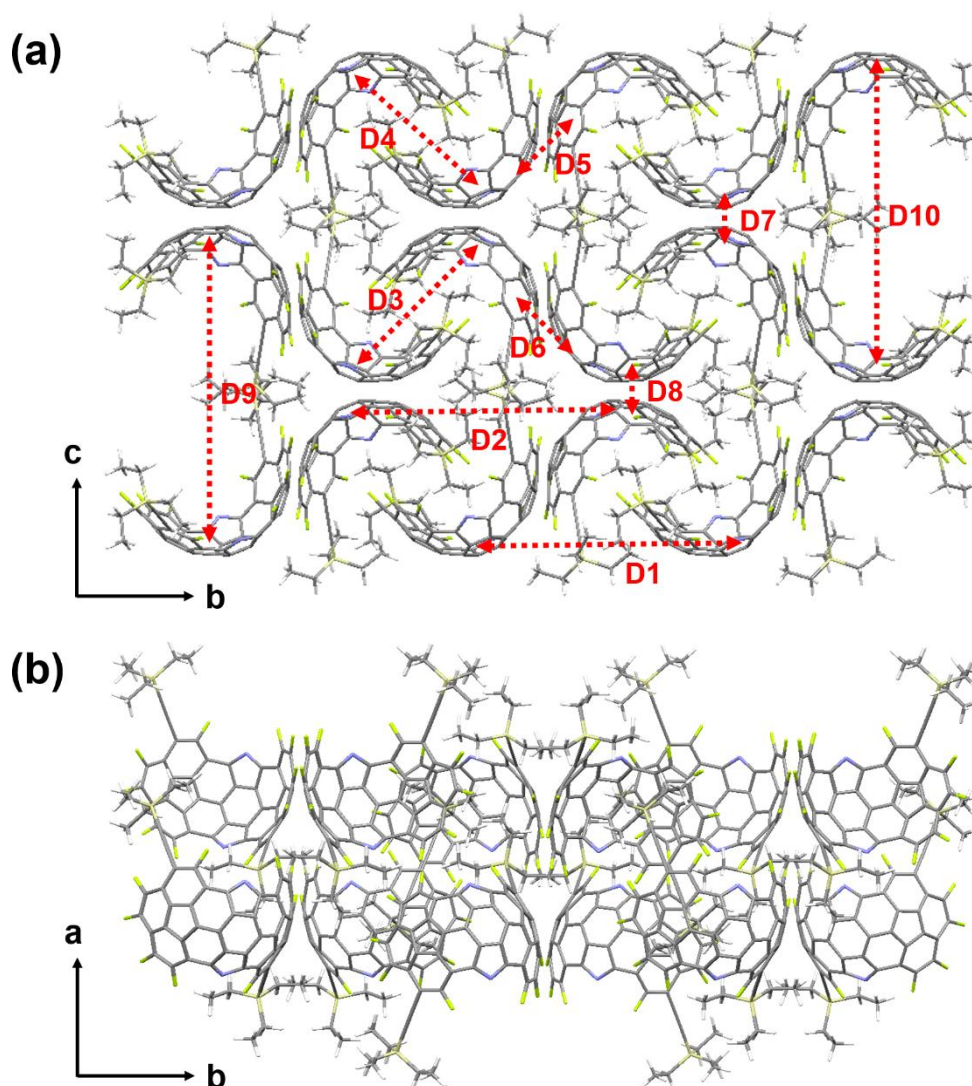


Figure S24. Crystal structure of DCP11-TES showing different conducting channels: (a) side view and (b) top view.

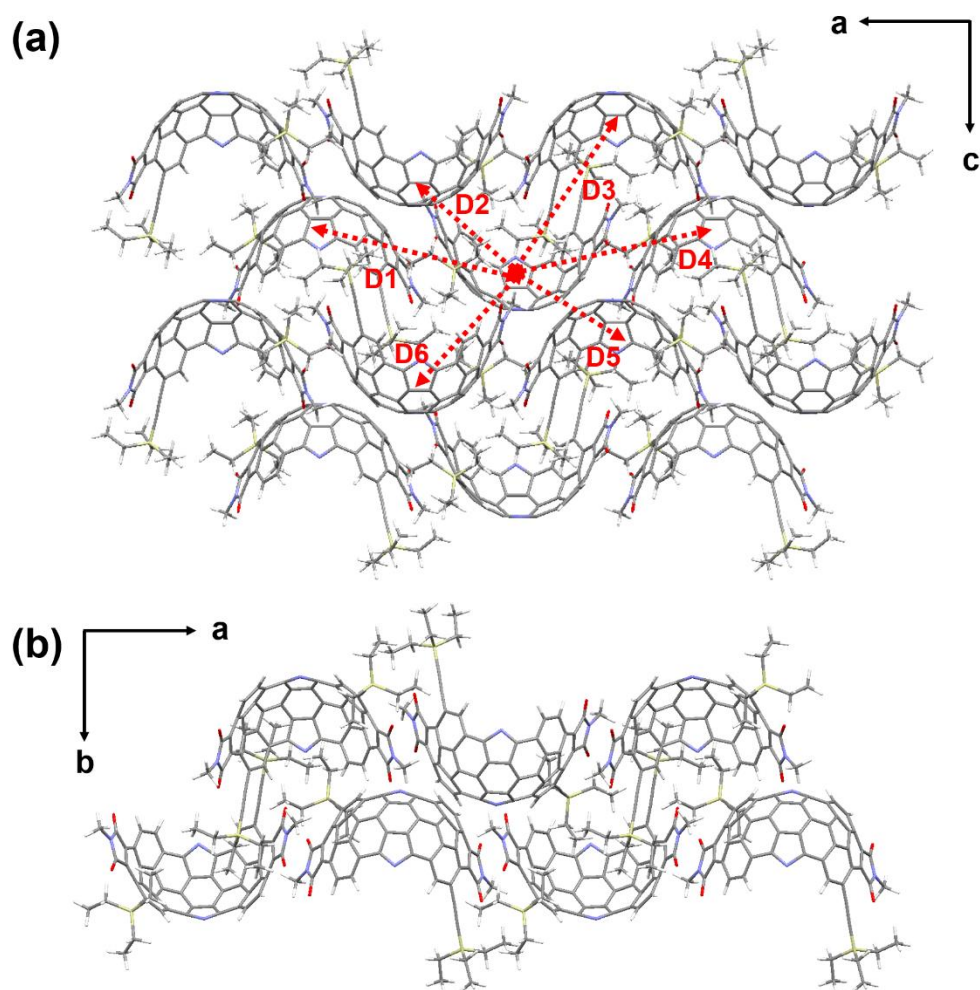


Figure S25. Crystal structure of DCPPI2-TES showing different conducting channels: (a) side view and (b) top view.

Table S8. The space groups and unit cell parameters of the crystal structures of corresponding DCP- and DCP-TES-based compounds.

Compound	Crystal System	Space group	Lattice parameters					
			a	b (Å)	c	α	β (Å)	γ
DCP-1	Orthorhombic	<i>Pna2₁</i>	7.34	18.99	9.94	90.0	90.0	90.0
DCP-2	Orthorhombic	<i>Pna2₁</i>	7.59	14.51	15.46	90.0	90.0	90.0
DCP-3	Orthorhombic	<i>P2₁2₁2₁</i>	14.52	17.18	8.03	90.0	90.0	90.0
DCP-4	Orthorhombic	<i>Pna2₁</i>	8.06	17.99	15.39	90.0	90.0	90.0
DCP-5	Orthorhombic	<i>Pna2₁</i>	8.18	13.65	24.52	90.0	90.0	90.0
DCP-6	Monoclinic	<i>P2₁/c</i>	15.81	14.74	8.53	90.0	97.69	90.0
DCP-7	Orthorhombic	<i>Pbcn</i>	21.63	8.48	23.64	90.0	90.0	90.0
DCP-8	Orthorhombic	<i>P2₁2₁2₁</i>	22.74	8.78	13.58	90.0	90.0	90.0
DCP-9	Monoclinic	<i>P2₁/c</i>	13.37	22.92	8.87	90.0	110.68	90.0
DCP-10	Orthorhombic	<i>Pna2₁</i>	12.33	11.09	17.57	90.0	90.0	90.0
DCP-11	Orthorhombic	<i>Pna2₁</i>	13.05	11.71	18.15	90.0	90.0	90.0
DCP-12	Orthorhombic	<i>Pna2₁</i>	26.46	11.23	10.91	90.0	90.0	90.0
DCP-TES-1	Orthorhombic	<i>Pbca</i>	41.19	21.03	8.72	90.0	90.0	90.0
DCP-TES-2	Orthorhombic	<i>Pbca</i>	8.03	54.84	18.54	90.0	90.0	90.0
DCP-TES-3	Orthorhombic	<i>Pbca</i>	32.97	34.16	8.34	90.0	90.0	90.0
DCP-TES-4	Orthorhombic	<i>Pbca</i>	7.60	18.07	73.32	90.0	90.0	90.0
DCP-TES-5	Orthorhombic	<i>P2₁2₁2₁</i>	19.52	20.55	13.69	90.0	90.0	90.0
DCP-TES-6	Orthorhombic	<i>Pbca</i>	27.18	12.37	27.08	90.0	90.0	90.0
DCP-TES-7	Orthorhombic	<i>Pbcn</i>	39.57	15.87	17.38	90.0	90.0	90.0
DCP-TES-8	Orthorhombic	<i>P2₁2₁2₁</i>	17.24	14.69	21.55	90.0	90.0	90.0
DCP-TES-9	Orthorhombic	<i>P2₁2₁2₁</i>	25.80	17.61	12.40	90.0	90.0	90.0
DCP-TES-10	Orthorhombic	<i>Pbca</i>	18.13	23.50	24.12	90.0	90.0	90.0
DCP-TES-11	Orthorhombic	<i>Pbca</i>	15.90	30.68	21.51	90.0	90.0	90.0
DCP-TES-12	Orthorhombic	<i>P2₁2₁2₁</i>	26.34	15.34	13.85	90.0	90.0	90.0

Table S9. The notable absorption wavelengths (λ_{abs}), oscillator strengths (f), excitation energies, and major spectral compositions of the DCPD and DCPD-TES compounds, simulated in the TD-DFT framework in dichloromethane solvent, using CAM-B3LYP/6-311G(d,p) level of theory.

Compound	states	λ_{abs} (nm)	f	energy (eV)	Major compositions
DCPD-1	S ₁	398.0	0.440	3.115	H→L (98%)
	S ₉	235.6	1.323	5.264	H-1→L (45%), H→L+2 (54%)
	S ₁₂	206.4	0.528	6.007	H-2→L+1 (59%), H-1→L+2 (25%)
DCPD-2	S ₁	450.1	0.662	2.754	H→L (98%)
	S ₉	254.7	0.551	4.867	H-3→L (26%), H-1→L+1 (53%)
	S ₁₈	209.4	0.786	5.922	H-4→L+1 (54%), H-2→L+4 (17%)
DCPD-3	S ₁	490.2	0.860	2.530	H→L (98%)
	S ₉	276.7	0.584	4.481	H-6→L (12%), H-2→L+4 (10%), H-1→L+2 (66%)
	S ₁₅	242.8	0.801	5.107	H-6→L (36%), H-1→L+3 (45%)
DCPD-4	S ₁	501.1	0.897	2.474	H→L (98%)
	S ₆	304.3	0.146	4.074	H-4→L (69%)
	S ₁₁	256.2	0.819	4.839	H-6→L (22%), H-1→L+2 (51%)
DCPD-5	S ₁	521.6	1.116	2.377	H→L (96%)
	S ₄	353.3	0.114	3.509	H→L+1 (80%)
	S ₆	319.3	0.178	3.883	H-3→L (66%), H→L+7 (10%)
	S ₁₅	277.9	1.314	4.461	H-1→L+2 (49%), H→L+3 (35%)
DCPD-6	S ₃	512.8	0.071	2.418	H-4→L (22%), H-2→L (67%)
	S ₅	412.1	0.361	3.009	H-5→L (27%), H-4→L (51%)
	S ₉	332.4	0.458	3.731	H-8→L (17%), H→L+1 (59%)
	S ₁₇	270.9	1.018	4.577	H-1→L+3 (66%)
DCPD-7	S ₃	523.3	0.071	2.370	H-3→L (24%), H-2→L (64%)
	S ₅	417.5	0.370	2.970	H-5→L (24%), H-3→L (51%)
	S ₁₀	338.6	0.543	3.661	H→L+1 (71%)
	S ₁₇	265.9	1.052	4.663	H-1→L+3 (71%)
DCPD-8	S ₅	414.4	0.177	2.992	H-5→L (56%), H-4→L (30%)

DCPP-9	S ₇	382.4	0.436	3.243	H-11→L (33%), H-4→L (44%)
	S ₈	357.8	0.592	3.466	H-1→L+2 (10%), H→L+1 (62%)
	S ₁₈	285.1	1.061	4.348	H-13→L (16%), H-1→L+3 (50%)
	S ₁	424.4	0.576	2.922	H→L (95%)
	S ₁₆	280.3	0.822	4.423	H-5→L+1 (50%), H-2→L+2 (33%)
DCPP-10	S ₁₉	253.6	0.923	4.889	H-1→L+4 (78%)
	S ₃	611.1	0.101	2.029	H-2→L (83%)
	S ₆	488.5	0.149	2.538	H-7→L (16%), H-6→L (71%)
DCPP-11	S ₉	377.5	0.178	3.284	H-8→L (52%), H-7→L (29%), H-6→L (10%)
	S ₁₃	323.6	0.614	3.831	H-10→L (25%), H→L+1 (13%), H→L+2 (44%)
	S ₅	585.5	0.101	2.117	H-4→L (87%)
	S ₆	520.9	0.169	2.380	H-6→L (78%), H-2→L (10%)
	S ₁₄	331.0	0.281	3.746	H-10→L (24%), H→L+1 (26%), H→L+2 (25%)
DCPP-12	S ₁₆	317.4	0.572	3.906	H-3→L+2 (14%), H-1→L+3 (22%), H-1→L+4 (10%), H→L+2 (27%)
	S ₂	876.8	0.035	1.414	H-1→L (92%)
	S ₃	614.4	0.107	2.018	H-2→L (79%)
	S ₆	496.1	0.174	2.499	H-6→L (77%)
	S ₉	377.0	0.519	3.289	H-12→L (26%), H-7→L (25%), H→L+1 (27%)
DCPP-TES-1	S ₁₅	334.0	0.486	3.712	H→L+3 (63%)
	S ₁	403.7	0.406	3.072	H→L (97%)
DCPP-TES-2	S ₆	267.3	2.841	4.638	H-2→L (32%), H-1→L+1 (20%), H→L+2 (34%)
	S ₁	457.6	0.604	2.710	H→L (97%)
	S ₈	277.1	1.460	4.475	H-3→L (13%), H-2→L (10%), H-1→L+1 (16%), H→L+2 (14%), H→L+3 (25%)
DCPP-TES-3	S ₁₀	266.5	0.639	4.652	H-4→L (13%), H-1→L+1 (25%), H→L+4 (33%)
	S ₁	494.0	0.797	2.510	H→L (97%)
	S ₁₀	285.1	1.371	4.349	H-2→L+1 (20%), H→L+3 (45%)
DCPP-TES-4	S ₁₉	245.8	1.024	5.045	H-6→L (23%), H-1→L+4 (47%)
	S ₁	506.8	0.846	2.446	H→L (97%)
	S ₆	332.8	0.432	3.725	H-4→L (34%), H-3→L (39%), H-1→L+1 (14%)
DCPP-TES-5	S ₉	287.2	0.557	4.318	H-8→L (23%), H-2→L+1 (21%), H→L+3 (24%)
	S ₁	526.0	1.022	2.357	H→L (96%)

DCPP-TES-6	S ₆	347.8	0.466	3.565	H-3→L (55%), H-2→L (10%)
	S ₁₆	281.9	0.857	4.398	H-2→L+2 (10%), H→L+3 (27%), H→L+4 (27%)
	S ₃	576.9	0.167	2.149	H-4→L (17%), H-2→L (71%)
	S ₄	482.2	0.531	2.571	H-5→L (30%), H-4→L (42%), H-2→L (23%)
DCPP-TES-7	S ₁₀	353.9	0.716	3.504	H→L+1 (63%)
	S ₁₈	299.1	0.537	4.145	H-16→L (34%), H-12→L (31%)
	S ₃	596.0	0.212	2.080	H-3→L (15%), H-2→L (72%)
	S ₄	498.0	0.489	2.490	H-5→L (30%), H-3→L (43%), H-2→L (21%)
DCPP-TES-8	S ₁₁	360.7	0.667	3.437	H→L+1 (65%)
	S ₁₉	295.6	0.728	4.194	H-17→L (28%), H-13→L (17%), H-2→L+2 (16%)
	S ₃	589.3	0.120	2.104	H-3→L (12%), H-2→L (75%)
	S ₄	490.8	0.506	2.526	H-5→L (21%), H-3→L (45%), H-2→L (18%)
DCPP-TES-9	S ₈	377.1	0.755	3.288	H→L+1 (68%)
	S ₁₇	305.1	0.544	4.064	H-9→L (32%), H-2→L+2 (13%), H-1→L+3 (11%)
	S ₁	426.4	0.556	2.908	H→L (93%)
	S ₇	337.2	0.241	3.677	H-6→L (12%), H-4→L (17%), H-3→L+1 (11%), H-2→L (16%), H-1→L+3 (11%)
DCPP-TES-10	S ₁₄	295.4	1.016	4.197	H-5→L+1 (40%), H-4→L+2 (25%), H-2→L (12%)
	S ₃	654.8	0.201	1.893	H-2→L (76%), H-1→L (11%)
	S ₆	516.1	0.244	2.403	H-8→L (21%), H-6→L (60%)
DCPP-TES-11	S ₁₂	344.6	0.730	3.598	H→L+1 (78%)
	S ₃	694.6	0.182	1.785	H-2→L (73%), H-1→L (14%)
	S ₅	598.5	0.103	2.072	H-4→L (87%)
DCPP-TES-12	S ₆	543.6	0.208	2.281	H-10→L (12%), H-6→L (66%)
	S ₁₂	352.6	0.499	3.516	H-16→L (23%), H-1→L+3 (12%), H→L+1 (15%), H→L+2 (15%)
	S ₃	688.8	0.238	1.800	H-2→L (66%), H-1→L (20%)
	S ₆	527.3	0.180	2.351	H-5→L (30%), H-4→L (56%)
	S ₁₁	382.6	0.538	3.241	H-1→L+2 (16%), H→L+1 (64%)

H: Highest occupied molecular orbital (HOMO); L: lowest unoccupied molecular orbital (LUMO).

Reference

- S1. Huang, J.-L.; Rao, B.; Kumar, M. P.; Lu, H.-F.; Chao, I.; Lin, C.-H. *Org. Lett.* **2019**, 21, 2504–2508.
- S2. BIOVIA, D. S., Materials Studio 2017. Dassault Systemes, San Diego Google Scholar 2017.
- S3. Debata, S.; Sahoo, S. R.; Khatua, R.; Sahu, S.; *Phys. Chem. Chem. Phys.* **2021**, 23, 12329-12339.
- S4. Li, H.; Bahuleyan, B. K.; Johnson, R. P.; Shchipunov, Y. A.; Suh, H.; Ha, C. -S.; Kim, I. *J. Mater. Chem.* **2011**, 21, 17938-17945.
- S5. Alberga, D.; Ciofini, I.; Mangiatordi, G. F.; Pedone, A.; Lattanzi, G.; Roncali, J.; Adamo, C. *Chem. Mater.* **2017**, 29, 673–681.